

Storm-Induced Circulation in Lunenburg Bay of Nova Scotia: Observations and Numerical Simulations

LIANG WANG, JINYU SHENG, ALEX E. HAY, AND DOUGLAS J. SCHILLINGER

Department of Oceanography, Dalhousie University, Halifax, Nova Scotia, Canada

(Manuscript received 16 May 2005, in final form 25 May 2006)

ABSTRACT

An extreme weather event (Hurricane Juan) made landfall in Nova Scotia, Canada, in September 2003. The storm produced an ~ 70 -cm storm surge and $\sim 40 \text{ cm s}^{-1}$ coastal currents in Lunenburg Bay, registered by a coastal observing system. A fine-resolution (60 m) coastal circulation model is used to examine the response of Lunenburg Bay to Hurricane Juan. The model is forced by local wind stress at the sea surface, and tides and remotely generated waves specified at model open boundaries. The model performance is assessed in terms of γ^2 , the variance of the model errors normalized by the observed variance. The model reproduces very well the observed surface elevations with γ^2 values of less than 0.05, and reasonably well the observed currents with γ^2 values between 0.2 and 1.1 in the bay during Hurricane Juan. The model–data comparisons demonstrate that the coastal circulation in the bay is significantly affected by local wind associated with the storm. The model results are also used to demonstrate the importance of nonlinear dynamics in the barotropic response of the bay to the storm.

1. Introduction

Coastal and shelf waters of Atlantic Canada are frequently affected by autumn and winter storms and occasionally by hurricanes (Smith and Schwing 1991). For example, in the early morning of 29 September 2003 Hurricane Juan made landfall along the south coast of Nova Scotia, roughly midway between Halifax and Lunenburg Bay (hereinafter LB) as a category-2 hurricane (on the Saffir–Simpson hurricane scale), with maximum sustained winds of 158 km h^{-1} and gusts to over 185 km h^{-1} (Levinson and Waple 2004). Hurricane Juan was the most damaging storm to hit Nova Scotia in more than a century, leading to the loss of several lives, millions of uprooted trees, and property damage worth at least \$100 million. Hurricane Juan also generated significant storm surges, shelf waves, and intense inertial currents on the Scotian Shelf (Sheng et al. 2006).

Many field programs have been conducted on the eastern Canadian shelf during the last two decades to investigate the coastal and shelf circulation in the re-

gion. As part of the Canadian Atlantic Storms Program (CASP), an intense oceanographic field program was undertaken on the inner Scotian Shelf in the winter of 1985/86 to examine the response of the shelf to Atlantic Ocean winter storms (Anderson and Smith 1989). In the early 1990s as part of a multidisciplinary research program called the Ocean Production Enhancement Network (OPEN), three separate field programs were conducted respectively on the Newfoundland–Labrador Shelf–Slope (de Young et al. 1993), on the West Bank of the Scotian Shelf (Griffin and Thompson 1996), and in LB and associated coves of Nova Scotia (Grant et al. 1993). A field program called the Canadian Search and Rescue Planning (CANSARP) experiment was carried out on the inner Scotian Shelf in 1996 to examine the wind-driven circulation and associated variability in the surface layers of the shelf (Sheng et al. 2001b; Thompson et al. 2003). A long-term monitoring program known as the Atlantic Zone Monitoring Program (AZMP) has been run since 1998 by the Department of Fisheries and Oceans of Canada for collecting and analyzing oceanographic data at several select locations and transects over the eastern Canadian shelf (Therriault et al. 1998).

Significant progress has also been made in last 20 yr in simulating storm-induced coastal and shelf circulations on the eastern Canadian shelf. Schwing (1992)

Corresponding author address: Dr. Jinyu Sheng, Department of Oceanography, Dalhousie University, Halifax, NS B3H 4J1, Canada.

E-mail: jinyu.sheng@dal.ca

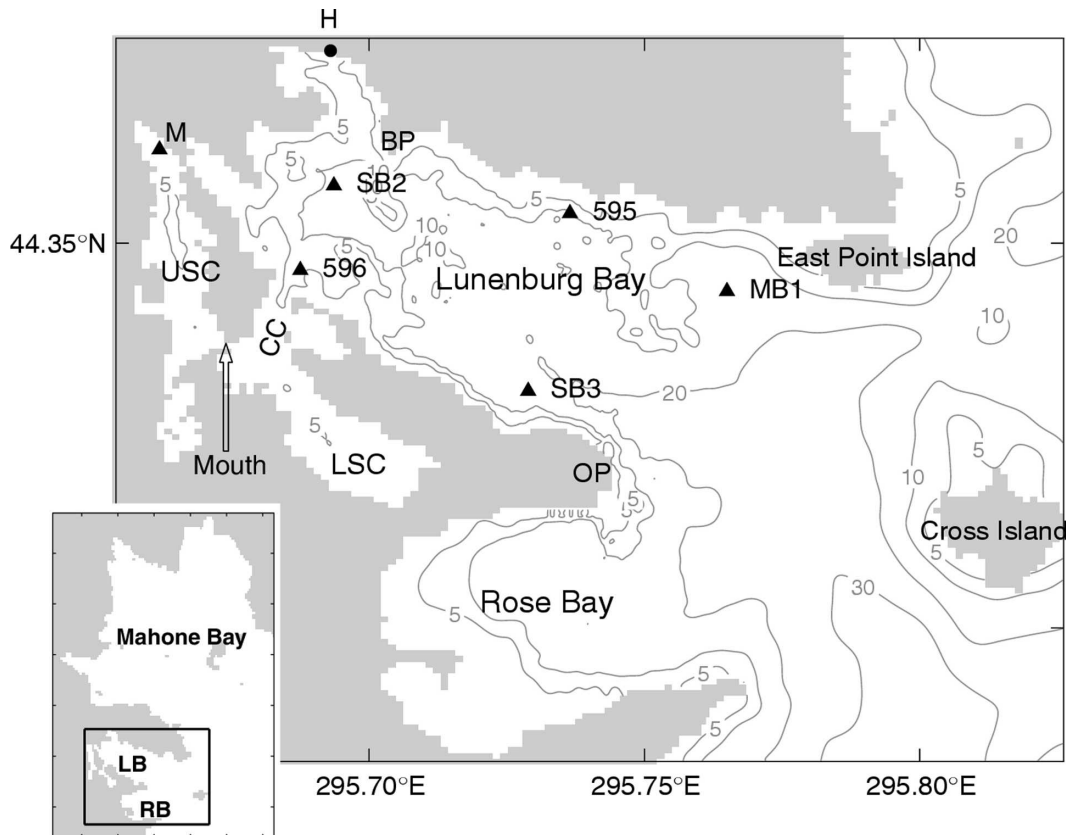


FIG. 1. Selected bathymetric features within the model domain of the Lunenburg Bay circulation model. Contours are labeled in meters. Abbreviations are used for Corkum's Channel (CC), Upper South Cove (USC), Lower South Cove (LSC), Oven Point (OP), and Lunenburg Harbour (H). The filled triangles denote the observation locations. Inset shows the coastal area of Mahone Bay, Lunenburg Bay (LB) and Rose Bay (RB).

studied the circulation on the Scotian Shelf in response to wind and remotely generated waves (RGW) using a time-harmonic, depth-integrated ocean circulation model. Greenberg et al. (1997) examined the barotropic circulation and pressure field response of the Scotian Shelf and Gulf of Maine to spatially uniform wind stress using a harmonic finite element model. Thompson and Sheng (1997) studied the subtidal circulation on the Scotian Shelf due to local wind stress and RGW during the winter of 1985/86 using a time-dependent, Galerkin spectral model. Tang et al. (1998) investigated the barotropic response of the Labrador and Newfoundland Shelves to a moving storm using a time-dependent, finite-difference model. Bobanovic and Thompson (2001) investigated the influence of local and remote winds on the sea level and circulation variability in the Gulf of St. Lawrence using a shallow-water equation, finite-difference model. Sheng et al. (2006) examined the upper ocean response of the Scotian Shelf and adjacent slope to Hurricane Juan using a nested-grid, primitive equation, finite-difference

ocean model. In this paper, we examine the main physical processes operating in LB during Hurricane Juan using the high-resolution (60 m), coastal circulation model developed recently by Sheng and Wang (2004).

In 2001, a multiagency initiative was undertaken to develop a relocatable marine environmental observation and prediction system, using data-assimilative and coupled models guided directly by real-time observations, for interdisciplinary research in the coastal regions of Atlantic Canada. The numerical modeling component of the full observation and prediction system was initiated in 2001. The prototype coastal observatory was established in the summer of 2002, in LB (Fig. 1; see also <http://www.cmep.ca/bay>; Safter 2002). One of the central scientific objectives of this initiative, and one of the primary justifications for adopting continuous, real-time observing approach, were to capture the response of the coastal ocean to episodic events, especially extreme events. Thus, it was serendipitous indeed when, in only its second year of operation, the observatory was operational when Hurricane Juan, the

most severe weather event to strike Nova Scotia in 100 yr, made landfall within 50 km of the site.

The arrangement of this paper is as follows. The next section discusses the oceanographic observations made in LB in September and October 2003. Section 3 summarizes the coastal circulation model and external forcings used in this study. Section 4 discusses the simulated circulation in LB during Hurricane Juan, and section 5 presents the model validation by comparing the model results with the observations. Section 6 discusses the dynamic balance and nonlinear interaction that affect the coastal circulation in LB during Hurricane Juan. Section 7 presents the model sensitivity to local wind forcing and vertical mixing. The final section is a summary and conclusion.

2. The ocean observing system in Lunenburg Bay

The LB coastal observing system was established in 2002. The core of the observing system consists of three solar-powered floating data acquisition nodes fore-and-aft moored in the central part of the bay. The locations of these three buoy-nodes are indicated in Fig. 1 by SB2, SB3, and MB1. Each buoy-node communicates with the shore station at Battery Point (BP in Fig. 1) via a wireless Ethernet link. The data are then transferred to Dalhousie University in Halifax over the internet in near-real time.

Each buoy node supports a suite of oceanographic and meteorological sensors. The data acquisition schedule involves powering up the instruments and acquisition-and-control computer on the buoy according to a preset schedule. In 2003, data were acquired in 10-min runs every half hour. (More details on the observing system can be found at the Web site <http://www.cmep.ca/bay>).

The sensors on each buoy node most relevant to this study included a pressure gauge and an upward-looking 1.5-MHz Sontek Acoustic Doppler profiler (ADP), both deployed on a bottom-mounted pod connected to the buoy by a power and communications cable. Also, an anemometer was mounted on each buoy at 3-m height.

The observed currents and surface elevations used in assessing the model hindcast skill in section 5 are partly based on the average values from the buoy node sensors for each data record; that is, the mean over the 10-min duration of each run. The ADPs acquired ensemble averages of 72 pings at 10-s intervals, and the run-mean velocities are an average over 4176 pings in total, using the 31 cm s^{-1} single ping accuracy stated by the manufacturer and our choice of 50-cm vertical bin width. The maximum velocities are thus expected to be

accurate to within $\pm 0.48 \text{ cm s}^{-1}$, assuming that errors in 4176 pings are statistically independent. (See also the last paragraph in this section for additional information on current measurements and their accuracy.) The pressure sensors were sampled at 0.25 Hz and these data were similarly run-averaged to remove any high-frequency variability due to surface gravity waves.

The wind speed and direction recorded by the anemometer were converted to Cartesian components, averaged over the 10-min duration of the run, and used to compute the mean wind speed and direction (Fig. 2). In 2003, the anemometer did not have an internal compass. Consequently there is additional uncertainty in the direction of local mean wind because any departure during a data run of the mean buoy orientation from its measured orientation (in calm conditions) is not known for the 2003 data. Buoy orientation compasses were added prior to the 2004 field season. The data from 2004 indicate that the standard deviations of the run-mean buoy orientations were $\pm 7.78^\circ$, $\pm 11.45^\circ$, and $\pm 24.11^\circ$ for SB2, SB3, and MB1, respectively.

The disk drive on each buoy had sufficient storage capacity for 7 days of data. Excess energy from the solar panels during the day was used to charge a bank of batteries mounted in the buoy hull, allowing data to be acquired both day and night. Fortunately, this combination of solar power and on-board data storage capacity allowed us to continue to collect data during the critical 2D period immediately following Hurricane Juan, while electrical power on land was being restored following widespread damage by the hurricane to the local power distribution system.

In addition to the buoy nodes, bottom-mounted pressure-temperature (PT) sensors are normally deployed at two locations M and H in Fig. 1. In 2003, data from these sensors are also acquired in near real time, and transmitted directly to Dalhousie University via a cellular telephone link (at site M) or via the internet (at site H). The PT sensor sampled at 0.8 Hz. Data records 20-min long were transmitted every 1/2 h. Run means were computed as for the buoy-node data stream.

Last, in anticipation of the autumn storm season, the observing system was augmented in mid-September 2003 by internally recording InterOcean S4 electromagnetic current meters. These instruments were deployed about 0.7 m above sea bottom on lead-ballasted aluminum frames at locations 595 and 596 in Fig. 1. The S4 current meters recorded 1-min averages of velocity and pressure (sampled at 2 Hz) every 4 min. Also, a bottom pod was not connected to the outermost buoy node, MB1, in 2003. Instead, the pod in this location was autonomous, and velocity profile data were obtained using an internally recording, 1200-kHz RD In-

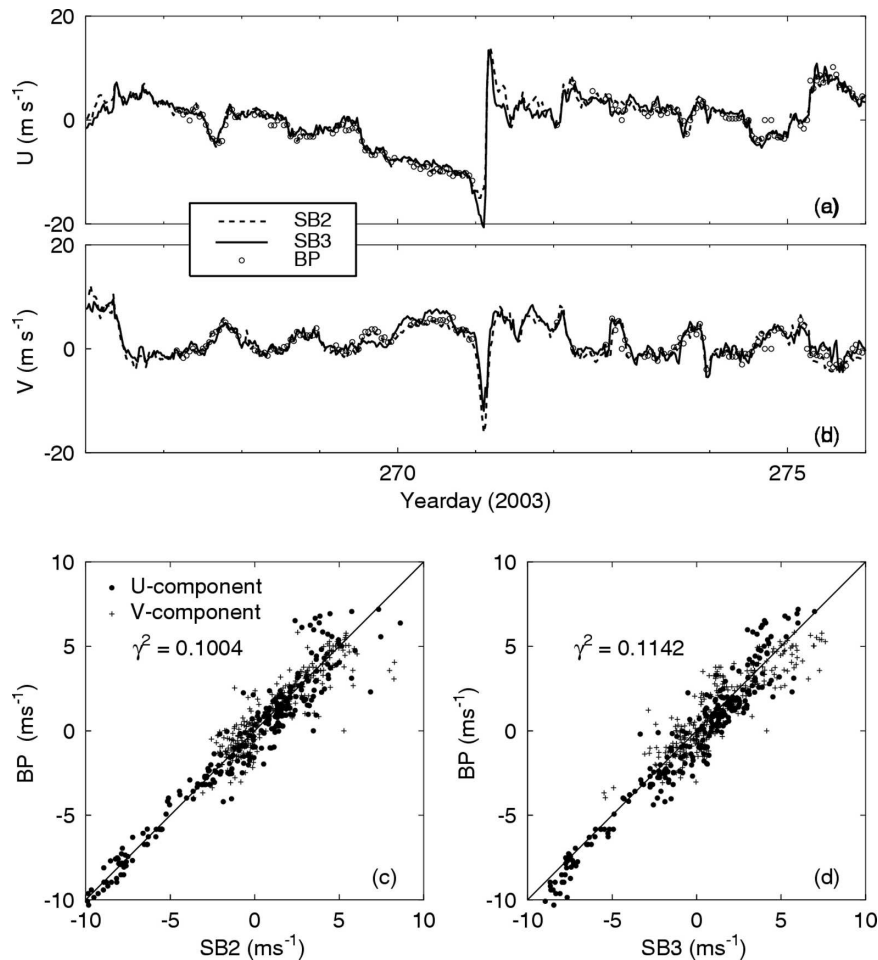


FIG. 2. Time series of (a) eastward and (b) northward components of observed wind speeds at 10-m height above the mean sea level at sites SB2, SB3, and at 10-m height above ground at Battery Point (BP), and scatterplots of (c) eastward and (d) northward components of the observed wind speeds at the three sites. Peak local winds during Hurricane Juan occurred at about 0230 UTC on yearday 271.

struments ADCP. The ADCP was set to acquire 35-ping ensemble-averaged profiles at 2-min intervals with 0.5-m vertical resolution. The single ping accuracy quoted by the manufacturer for these settings is 6.1 cm s^{-1} , giving an estimated accuracy for the 1/2-h averaged velocity data from this instrument of 0.27 cm s^{-1} .

3. The coastal circulation model and external forcing

A three-dimensional (3D) coastal circulation model developed by Sheng and Wang (2004) for LB is used in this study. The coastal model of LB is based on the primitive equation, finite-difference, z -level ocean circulation model known as Canadian Version of Diecast

(CANDIE; Sheng et al. 1998; <http://www.phys.ocean.dal.ca/programs/CANDIE>). The rigid-lid version of CANDIE has successfully been used to simulate the subtidal circulation forced by wind over an idealized coastal canyon (Sheng et al. 1998), nonlinear dynamics of the Gaspé Current (Sheng 2001), wind-driven circulation over a stratified coastal embayment (Davidson et al. 2001), large-scale circulation in the northwestern Atlantic Ocean (Sheng et al. 2001a), and seasonal circulation in the western Caribbean Sea (Sheng and Tang 2003, 2004). The free-surface version of CANDIE has successfully been used to simulate the tidal circulation in the Gulf of St. Lawrence (Lu et al. 2001), and nonlinear tidal dynamics in LB (Sheng and Wang 2004).

The governing equations for LB coastal circulation model are described in the appendix and the basic model setup is described in Sheng and Wang (2004).

Temperature and salinity in this study are set to be invariant in time and space (i.e., barotropic run). The domain of the coastal model (Fig. 1) covers LB, Upper South Cove (USC) and Lower South Cove (LSC), with a horizontal resolution of 60 m. The model has 22 z levels with a vertical resolution of 1 m, except for 3.6 m for the top z level and 4.85 m for the last four z levels near the bottom. The model time step is 17 s. The model uses the horizontal mixing scheme of Smagorinsky (1963) and a quadratic bottom stress parameterization with a spatially varying drag coefficient, which is set to 1.0×10^{-2} in the center of Corkum's Channel, and decreases exponentially to the conventional value of 3.0×10^{-3} with an e -folding distance of 2 km (Sheng and Wang 2004). For the vertical eddy viscosity coefficient K_m , we follow Davies et al. (1998) and set

$$K_m = K_t + K_w, \quad (1)$$

where K_t is the vertical eddy viscosity coefficient induced by the depth mean (tidal) flow and K_w is the vertical eddy viscosity coefficient induced by the surface wind stress. Because LB is relatively shallow and the bottom boundary layer thickness in the region is limited by the local water depth, we follow Davies (1993) and specify K_t as

$$K_t = K_o h |\mathbf{U}_d| \phi(z), \quad (2)$$

where K_o is a dimensionless coefficient set to 3.0×10^{-3} , h is the local water depth, $|\mathbf{U}_d|$ is the magnitude of the depth-mean horizontal velocity, and $\phi(z)$ is a prescribed vertical structure function, which is unity from the surface to $z = -0.8h$ and then decreases linearly to 0.01 at bottom $z = -h$ (Davies 1993). We follow Csanady (1982) and specify K_w as

$$K_w = \frac{0.1 |\boldsymbol{\tau}_s|}{\rho f R_e}, \quad (3)$$

where $|\boldsymbol{\tau}_s|$ is the magnitude of the surface wind stress vector, f is the Coriolis parameter, ρ is the density of water, and R_e is an eddy Reynolds number and is set to 20 (Csanady 1982). Although the linear combination of the vertical viscosity coefficient presented in (1) does not have a firm physical basis, it includes the effect of vertical eddy mixing originating from both the tidal flow and local wind forcing (Davies et al. 1998).

The following boundary conditions are used in the LB model. At the model lateral closed boundaries, the no-slip and zero normal flow conditions are applied to the horizontal currents. At the model open boundaries, the radiation condition suggested by Davies and Flather (1978) is used:

$$u_B = u_t + u_s + \frac{c}{h} (\eta_B - \eta_t - \eta_s), \quad (4)$$

where η_B and u_B are the model-calculated surface elevation and normal flow at the open boundaries, η_t and u_t are the tidal input of surface elevation and normal currents at the open boundaries, η_s and u_s are the surface elevation and normal currents associated with the remotely generated waves, and c is the phase speed. We follow Sheng and Wang (2004) and set $c = 0.16(gh)^{1/2}$.

Three types of model forcings are used in this study: 1) local wind forcing in LB, 2) tides, and 3) remotely generated waves. The latter two propagate into LB through the model open boundaries. The local wind forcing is based on the wind observations made in LB during a 10-day period from 24 September (day 266) to 3 October (day 275) 2003. Since the observed wind speeds at sites SB2 and SB3 in LB are highly similar (Fig. 2), the wind stresses at these sites, converted from observed wind speeds based upon the bulk formula of (Large and Pond 1981), are averaged to provide spatially uniform (but time-dependent) local wind forcing for the model. Figures 3a,c demonstrate that the local wind forcing in LB was relatively weak during the 10-day period, except for 29 September (day 271). The wind forcing increased with time in the early morning of day 271, and reached a maximum of about 1.1 Pa ($1 \text{ Pa} = 1 \text{ N m}^{-2}$) at 0230 UTC (all times in this study are in UTC), associated with Hurricane Juan.

Since there were no direct measurements of tidal currents u_t and surface elevation η_t along the model open boundaries during the study period, we approximate the tidal forcing at the model open boundaries by spatially uniform tidal surface elevation η_t and setting $u_t = u_{B-1}$, where u_{B-1} is the model-calculated (tidally forced) normal current at grid points closest to the open boundaries (i.e., gradient radiation condition; Chapman 1985). The spatial uniformity assumption of η_t is reasonable since the typical length of the model open boundaries is less than 10 km, which is very small in comparison with typical wavelengths of several hundreds to thousands kilometers for tidal waves. We determine η_t using the simplified incremental approach (SIA) from the tidal sea level prediction η_h^c at Lunenburg Harbour, which was made by the Canadian Hydrographic Service (CHS) using more than 60 tidal constituents determined from the historical sea level observations at the harbor. A detailed discussion of the SIA was described in Sheng and Wang (2004) and only a brief description is given as follows. Basically, we first integrate the coastal circulation model by setting η_t to η_h^c . We then calculate the transfer function (i.e., differences in magnitude and phase) between the model-calculated (η_h^m) and CHS predicted (η_h^c) surface elevations at Lunenburg Harbour. We use this transfer function to update η_t and integrate the coastal circulation

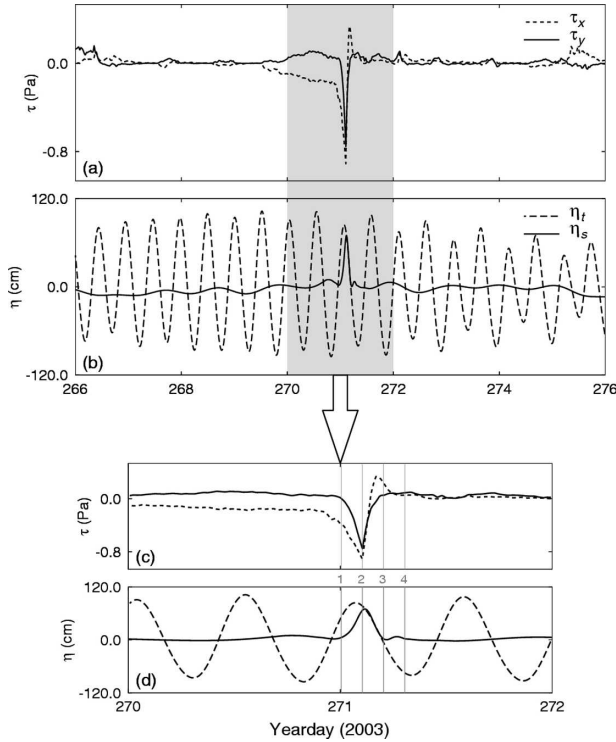


FIG. 3. Time series of three types of model external forcings: (a), (c) the eastward (τ_x) and northward (τ_y) components of surface wind stress in Lunenburg Bay, and (b), (d) surface elevations at model open boundaries to represent tidal forcing (η_t , dashed) and remotely generated waves (η_s , solid). The times marked by four light gray lines in (c) and (d) labeled 1–4 are chosen to present the model results.

model again with the updated η_t . We repeat the above procedure if the model-calculated η_t^m does not agree with η_t^c . For the barotropic tidal circulations in LB, we found that one iteration of the above procedure is sufficient to determine η_t from η_t^c .

Hurricane Juan generated a significant surge of water (i.e., storm surge) along the Atlantic coast of central Nova Scotia in the early morning of day 271. The maximum storm surge of about 150 cm was measured in Halifax harbor, of which about 40 cm was due directly to the atmospheric pressure (or the inverse barometer effect; Gill 1982). In this study, we consider only the adjusted sea level, which is the total sea level with the inverse barometer effect removed. The localized storm surge generated by Hurricane Juan propagated southwestward along the south coast of Nova Scotia as RGW. To represent the propagation of an RGW into Lunenburg Bay through the model open boundaries, we set η_s in (4) to be spatially uniform along the model open boundaries, and u_s to be the model-calculated (RGW forced) normal currents at the grid points closest to the open boundaries, in the same way as the tidal

TABLE 1. List of eight numerical experiments driven by different combinations of tidal forcing (TF), local wind forcing (LWF), and remotely generated waves (RGW) with different model dynamics; CR stands for control run.

Name of run	External forcing
Exp-A (CR)	TF + LWF + RGW
Exp-B	TF only
Exp-C	LWF only
Exp-D	RGW only
Exp-E	Same as in Exp-A, except that observed winds at SB2 are used
Exp-F	Same as in Exp-A, except that observed winds at SB3 are used
Exp-G	Same as in Exp-A, except that $K_m = K_t$
Exp-H	Same as in Exp-A, except that $K_m = K_w$

forcing discussed above. We estimate η_s from the observed surface elevations converted from the bottom pressure measurements at site SB2 in LB in three steps as follows. First, we run the coastal model with tides and local wind forcing to generate model-calculated surface elevations (forced by tides and local wind forcing) at SB2. Second, we calculate the differences between the observed and model-calculated surface elevations at SB2 and use these differences to represent the RGW-forced surface elevations at SB2. Third, we estimate η_s from the RGW-forced surface elevations at SB2 (after low-pass filtering to eliminate any additional tidal components) using again the ISA described above by assuming the spatial uniformity of η_s along open boundaries of the LB model. Figures 3b,d demonstrate that the RGW-forced η_s was relatively small before day 271 and increased significantly with time in the early morning of day 271. After reaching a peak value of 75 cm at 0300 UTC, η_s decreased quickly with time and remains small after day 271.5. It should be noted that the spatial uniformity assumption of η_s along the model open boundaries is reasonable, but less accurate than that for η_t since wavelengths of coastal trapped waves on the Scotian Shelf are much shorter than those of tidal waves.

4. Storm-induced circulation during Hurricane Juan

We integrate the LB coastal model for 10 days from 24 September (day 266) to 3 October (day 275) 2003, with three types of external forcings shown in Fig. 3 (referred to as the control run or Exp-A; see Table 1). Since the model is spun up from rest, the model results in the last 9 days are presented in this study.

Figure 4 shows the evolution of simulated surface elevations and currents in the early morning of 29 Sep-

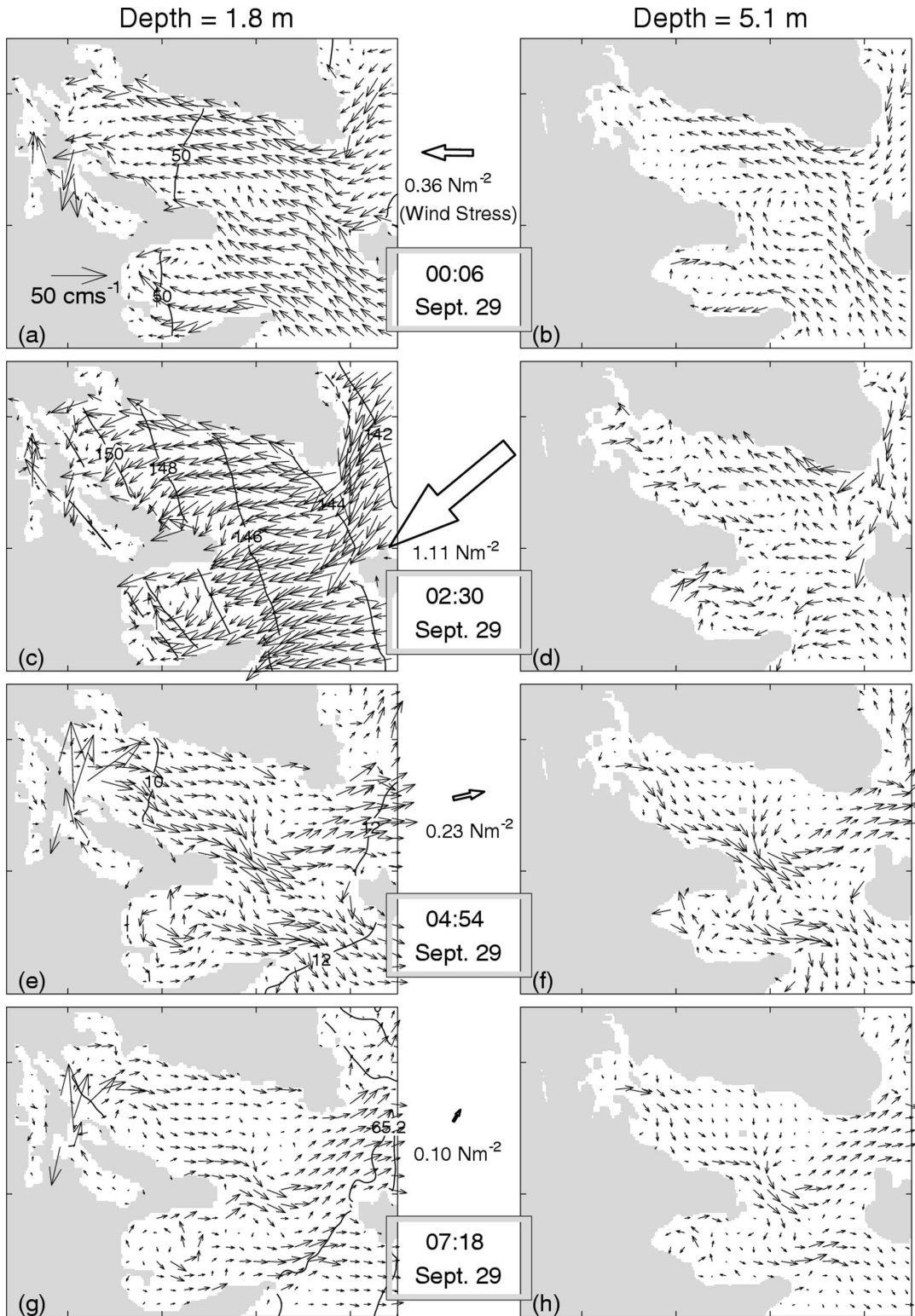


FIG. 4. Model experiment A (control run) results: simulated surface elevations, near-surface (1.8 m) currents, and subsurface (5.1 m) currents at (a), (b) 0006, (c), (d) 0230, (e), (f) 0454, and (g), (h) 0718 UTC 29 Sep (day 271) 2003. Contour interval for surface elevations is (a), (c), (e) 2 and (g) 0.5 cm. Velocity vectors are plotted at every eighth model grid point.

tember (day 271) 2003 when Hurricane Juan made landfall. At 0006 UTC, the local wind stress in LB was about 0.4 Pa and roughly westward (Figs. 4a,b). The simulated surface elevations at this time are spatially uniform and about 50 cm in LB. The near-surface (1.8 m depth) circulation at this time (Fig. 4a) is characterized by a spatially uniform northwestward inflow of about 15 cm s^{-1} over eastern LB, and a narrow inshore jet running northwestward along the west shoreline of LB. The northwestward currents and the inshore jet merge over northwestern LB and form a strong jet (about 40 cm s^{-1}) to flow southwestward into LSC through Corkum's Channel. The subsurface (5.1 m) circulation in LB (Fig. 4b) has similar circulation features as those at 1.8 m, except for smaller magnitudes. The subsurface currents are about 10 cm s^{-1} over eastern LB and much weaker over western LB at this time. Figures 4a,b also show an anticyclonic (clockwise) circulation in Rose Bay.

The local wind stress in LB veered cyclonically as Hurricane Juan passed by (since the study region was located to the left of the storm track). The wind forcing turned roughly southwestward and reached a maximum value of about 1.1 Pa at 0230 UTC (day 271.104). The simulated sea surface elevations in LB rise to about 145 cm at this time, with large horizontal changes of about 8 cm from the southeast part of the entrance to the northwestern corner of LB (Fig. 4c). The simulated near-surface circulation at this time is characterized by strong and roughly westward currents of about 30 cm s^{-1} over eastern LB and in the deep waters outside of LB. These westward currents turn gradually southwestward to flow onshore over western LB. The near-surface flow in Corkum's Channel remains southwestward, but slightly weaker than that at 0006 UTC. The subsurface circulation at 0230 is very similar to that at 0006 UTC, except that the inshore jet along the west shoreline of LB reverses its direction and runs southeastward at this time (Fig. 4d).

The local wind forcing decreased significantly to about 0.23 Pa and was roughly eastward at 0454 UTC (Figs. 4e,f). The simulated sea surface elevations in LB fall to 10 cm at this time (Fig. 4e), with horizontal changes of about 2 cm from the outer bay to the inner bay. The near-surface circulation in the bay, in response to the relaxation of the local wind forcing, is characterized by a strong outflow of about 20 cm s^{-1} over western LB and an intense jet of about 75 cm s^{-1} , which flows northeastward from LSC to inner LB through Corkum's Channel. The near-surface currents over eastern LB also flow out of the bay, but with smaller amplitudes. The subsurface currents in LB at 0454 UTC have similar circulation features as the near-surface

currents in LB, with a strong outflow of about 10 cm s^{-1} over western LB and weaker outer flow over eastern LB.

The local wind forcing in LB decreased further to 0.1 Pa and was roughly northeastward at 0718 UTC (Figs. 4g,h). The simulated surface elevations are spatially uniform and about -65 cm in LB (Fig. 4g). The simulated circulation in the top 5 m in LB at this time is characterized by a weak outflow of about 5 cm s^{-1} over western LB, and a strong northeastward jet emanating from Corkum's Channel to inner LB.

To examine the role of tidal forcing and local wind forcing in generating circulation in the bay during Hurricane Juan, we conduct two additional numerical experiments by integrating the coastal model with the tidal forcing only in the first experiment (Exp-B; Table 1; Fig. 5) and the local wind forcing only in the second experiment (Exp-C; Table 1; Fig. 6). Other model parameters are the same as in the control run. A comparison of surface elevations in Figs. 4–6 indicates that the surface elevations in the control run of about 50 cm at 0006 UTC are generated largely by the tidal forcing (about 45 cm). At 0230 UTC, the high surface elevations of about 145 cm in the control run (Fig. 4c) are generated by the combination of tidal forcing (about 83 cm; Fig. 5c) and RGW (about 60 cm; Fig. 3). The local wind contributes less than 10 cm of surface elevations in the bay at this time (Fig. 6c). The positive sea surface elevations of about 10 cm in LB at 0454 UTC in the control run are explained largely by tides and waves generated remotely by Hurricane Juan, while the negative sea surface elevations of about -65 cm at 0718 UTC are mainly generated by the tidal forcing. Although the local wind forcing plays a very minor role in generating the total sea level rise/fall in LB during Hurricane Juan, it produces significant sea level gradients in the bay, which are dynamically important. Indeed, the maximum across-bay sea surface elevation difference is near 10 to 12 cm produced by the model in both the control run and Exp-C (forced by the local wind stress only).

A comparison of model-calculated currents shown in Figs. 4–6 also demonstrates that the coastal currents in the bay at 0060 UTC in the control run are generated by the combination of the tidal and local wind forcing, whereas the southwestward jet in Corkum's Channel is largely generated by the tidal forcing. At 0230 UTC, the local wind-forced currents are very strong (Figs. 5c,d) and comparable to those in the control run (Figs. 4c,d). By comparison, the tidally forced currents at this time are very weak (Figs. 6c,d). At 0454 UTC, the local wind forcing is relatively weak, and the combination of the tidal forcing and pressure gradients produced by the wind forcing in the recent past is responsible for strong

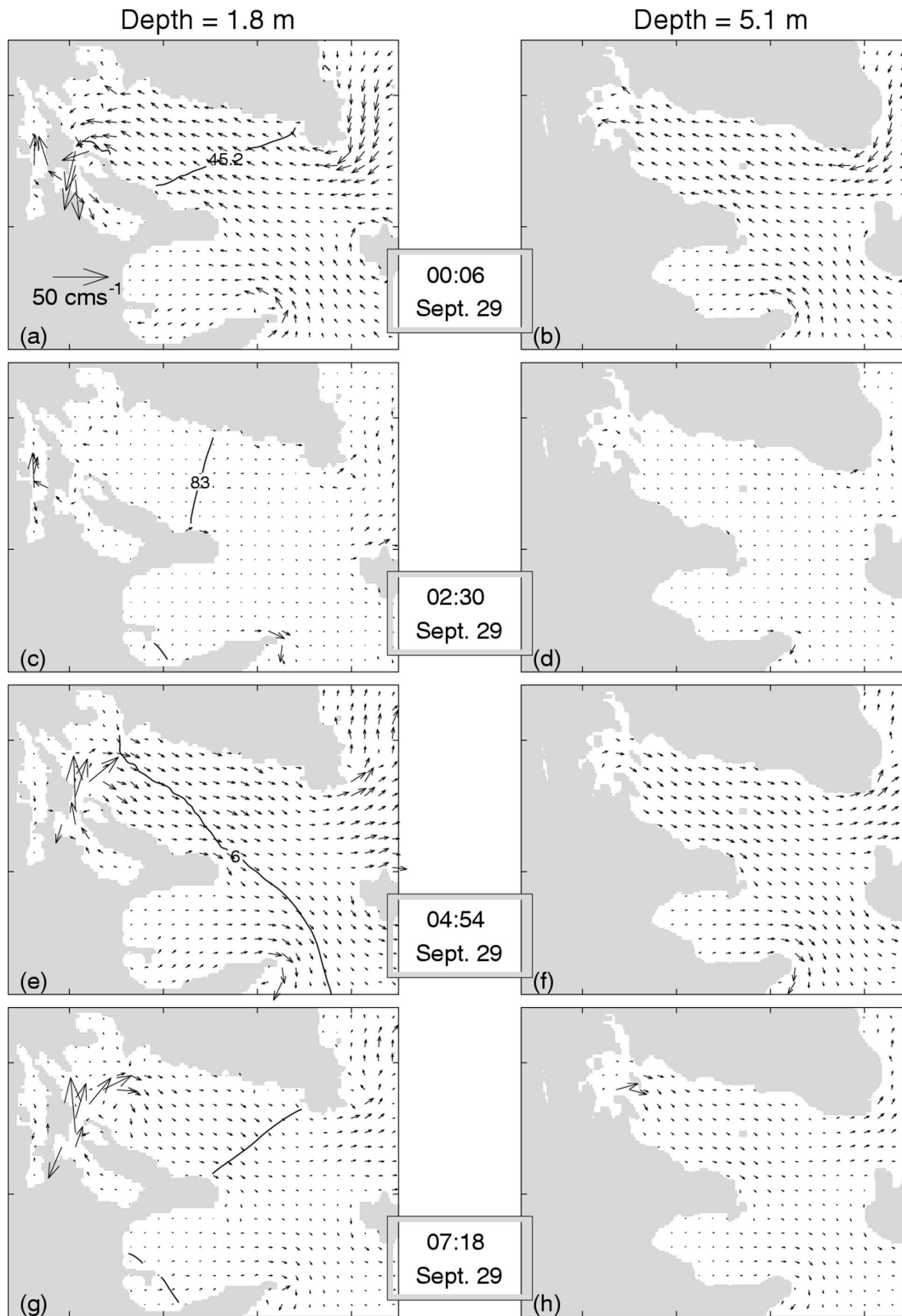


FIG. 5. Model experiment B (tidal forcing only) results: surface elevations, near-surface (1.8 m) currents, and subsurface (5.1 m) currents at (a), (b) 0006, (c), (d) 0230, (e), (f) 0454, and (g), (h) 0718 UTC 29 Sep (day 271) 2003. Velocity vectors are plotted at every eighth model grid point.

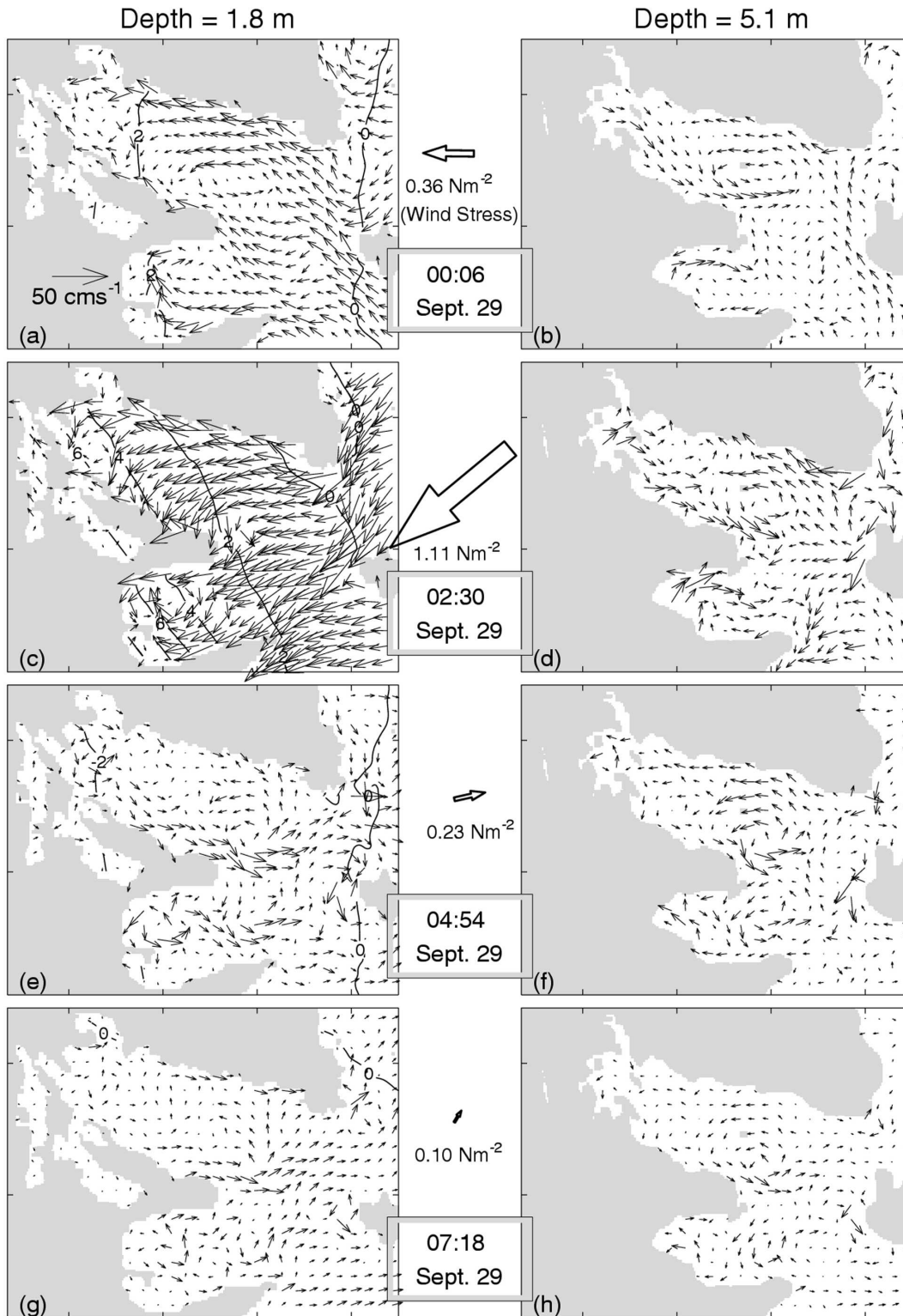


FIG. 6. Model experiment C (local wind forcing only) results: surface elevations, near-surface (1.8 m) currents, and subsurface (5.1 m) currents at (a), (b) 0006, (c), (d) 0230, (e), (f) 0454, and (g), (h) 0718 UTC 27 Sep (day 271) 2003. Contour interval for surface elevations is 2 cm. Velocity vectors are plotted at every eighth model grid point.

outflow over western LB and strong outflow from LSC to inner LB through Corkum's Channel at this time (see more discussion of pressure gradient terms in section 6; Fig. 12). At 0718 UTC, the spatially varying currents in LB are produced by the combination of the tidal forcing and pressure gradients (Figs. 4–6g,h) and the jetlike flow emanating from Corkum's Channel to inner LB is generated mainly by the tidal forcing (Fig. 5g).

5. Assessment of the model hindcast skill

We validate the model performance by comparing the model results in the control run (Exp-A) with the observations made in LB during the 9-day period from day 267 (25 September) to day 275 (3 October) in 2003. We follow Thompson and Sheng (1997) and quantify the model hindcast skill in terms of the γ^2 value defined as

$$\gamma^2 = \text{Var}(O - M) / \text{Var}(O), \quad (5)$$

where O and M represent the observed and model-calculated variables, respectively, such as surface elevations and currents in this study, and Var represents the variance. Physically, γ^2 represents the ratio of variance of the model hindcast errors (i.e., differences between observations and model results) to the variance of the observations. It is clear that the smaller γ^2 is, the better is the model hindcast skill. In the case of $\gamma^2 = 0$, the model results fit observations perfectly. In the case of γ^2 exceeding unity, the variance of the observed variable increases with the subtraction of the model hindcasts from the observations.

a. Surface elevation

Figure 7 compares the observed and simulated surface elevations at four sites in the study region during a 9-day period from 25 September to 3 October 2003. The γ^2 values for the simulated surface elevations at three LB sites SB2, SB3, and H are about 0.006–0.01 (Figs. 7a–c), indicating that more than 98% of the total variance of the observed surface elevations at the three sites is accounted for by the model results. This suggests that during this period the coastal model has significant hindcast skills in simulating the time evolution of surface elevations in LB forced by tides, RGW, and local wind forcing.

The γ^2 value for surface elevations at site M in Upper South Cove (Fig. 7d) is about 0.04, which is small but slightly larger than the γ^2 values at the three LB sites. As shown in Fig. 1, Upper South Cove is linked to Lower South Cove through a narrow mouth of about 60

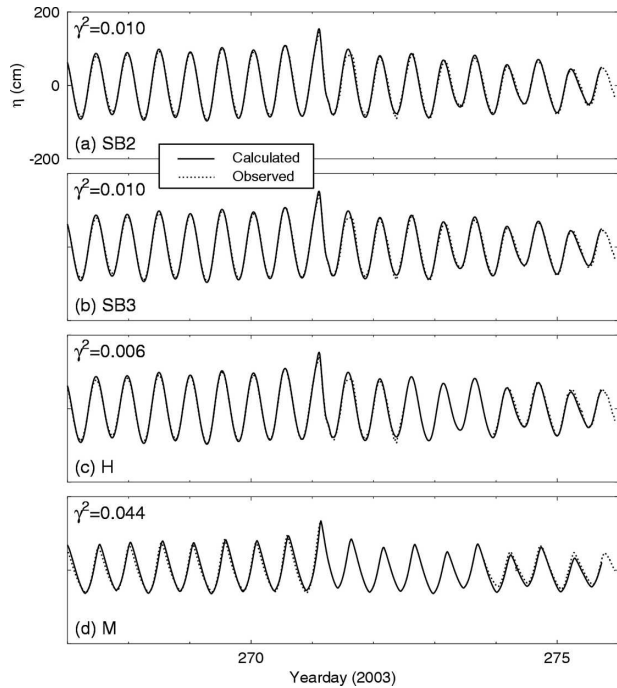


FIG. 7. Time series of observed and simulated sea surface elevations at sites (a) SB2, (b) SB3, and (c) H in Lunenburg Bay, and at site (d) M in Upper South Cove.

m wide and 3 m deep. Previous studies (Thompson et al. 1998; Sheng and Wang 2004) demonstrated that this narrow mouth, together with Corkum's Channel connecting LSC to LB, plays a very important role in determining the tidal circulation in inner LB and the two coves. Although the narrow mouth is not well resolved by the model with a horizontal resolution of 60 m, the model explains about 96% of the total variance of the observed surface elevations at site M in USC during this 9-day period, indicating that the model has reasonable skills in simulating the horizontal transport of waters through both the narrow mouth and Corkum's Channel.

Tidal harmonic analysis of the observed and simulated surface elevations (Fig. 7) indicates that tides with more than 30 tidal constituents (including M_2 , S_2 , K_1 , O_1 , etc.) explain over 99% and 96% of the total variance of observed and simulated surface elevations in LB and Upper South Cove, respectively. Therefore, the tidal forcing plays a dominant role in generating surface elevations at the four sites in LB and USC. (We obtain the same conclusion from the tidal analysis of observed and simulated surface elevations during one-month period from 20 September to 20 October 2003).

To validate the model hindcast skill in simulating nontidal surface elevations (i.e., the adjusted sea levels) in LB and USC, we compare the observed and simu-

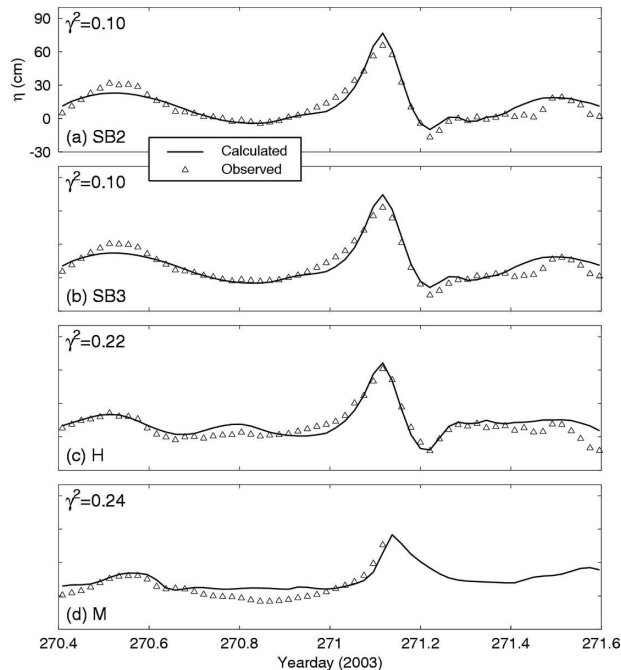


FIG. 8. Time series of observed and simulated nontidal sea surface elevations at sites (a) SB2, (b) SB3, and (c) H in Lunenburg Bay, and at site (d) M in Upper South Cove.

lated nontidal surface elevations at the four sites from day 270.4 to 271.6 in Fig. 8. The observed nontidal surface elevations at the three LB sites have similar temporal variations and are roughly in phase during this period, which are characterized by a rapid nontidal sea level rise to about 70 cm at day 271.113 (0243 UTC), followed by a quick sea level fall after reaching the maximum. The observed nontidal surface elevations at the three sites also have smaller maximum values of about 30 cm at day 270.528 before Hurricane Juan. Figure 8 shows that the simulated nontidal surface elevations agree well to the observations at three LB sites. At site M in Upper South Cove, there were no subsurface pressure measurements after day 271.16 because of the power failure (Fig. 8d). Before this time, the observed nontidal surface elevations at M in USC have similar temporal variations as those at the three sites in LB, except for smaller amplitudes and a phase lag of about 20 min (LB leading). The simulated nontidal surface elevations at site M have similar temporal variations as the observations at this site. The calculated γ^2 values are 0.10 at site SB2 and SB3, 0.22 at site H, and 0.24 at site M, which are small in general but larger than the γ^2 values for the total sea levels, indicating that the high-resolution LB model performs slightly less well in simulating the nontidal surface elevations than the tidal components, mainly because of the uniformity assump-

tion of η_s along the model open boundaries. It should be noted that the observed nontidal surface elevations at site SB2 have been used to determine the boundary conditions (η_s) associated with the remotely generated waves.

b. Currents

We next assess the model hindcast skill in simulating the three-dimensional (3D) currents in LB. Figure 9 shows time series of observed and simulated currents at three different depths of sites SB2, SB3, and MB1 during the 9-day period. The observed currents at the three sites possess typical tidal currents before and after the storm, with large wind-driven currents associated with Hurricane Juan in the early morning of day 271. The observed currents at the three sites also have low-frequency variabilities during a 3-day period from day 269 to 272 (middle and lower panels of Fig. 9). The LB coastal model reproduces the observed currents reasonably well, particularly the eastward components, at three different depths of the three sites. The model also reproduces reasonably well the extreme currents associated with Hurricane Juan at SB2 and SB3 in the early morning of day 271. The range of γ^2 values is about 0.79–1.04 (0.70–1.04) for the eastward (northward) components of the simulated currents at SB2; about 0.20–0.35 (0.42–0.61) for the eastward (northward) components at SB3; and about 0.64–0.93 (0.49–0.58) for the eastward (northward) components at MB1.

In comparison with the γ^2 values for the simulated surface elevations in LB, the coastal model simulates less well the observed currents in LB. This is not surprising since currents are much more sensitive to small-scale features of local bathymetry than sea surface elevations. Topographic features with horizontal scales less than 100 m in the study region are not well represented in the model mainly because of the model horizontal resolution of 60 m. Other factors that could affect the model performance in simulating the 3D currents include the accuracy of the model topography and external forcings, baroclinic effects in the bay, and model subgrid-scale mixing parameterizations. The 60-m model topography was constructed using Barnes' algorithm from several different data sources, including 40-m gridded topography made by Sturley et al. (1993) for the middle and inner LB and adjacent two coves; and 100-m gridded topography interpolated from the CHS charts for outer LB and outside areas of LB. In the model sensitivity studies presented in section 7, we will demonstrate that the strength and path of the outflow jet emanating from Corkum's Channel to inner LB are sensitive to the local wind forcing. We will also show that the model currents are sensitive to the ver-

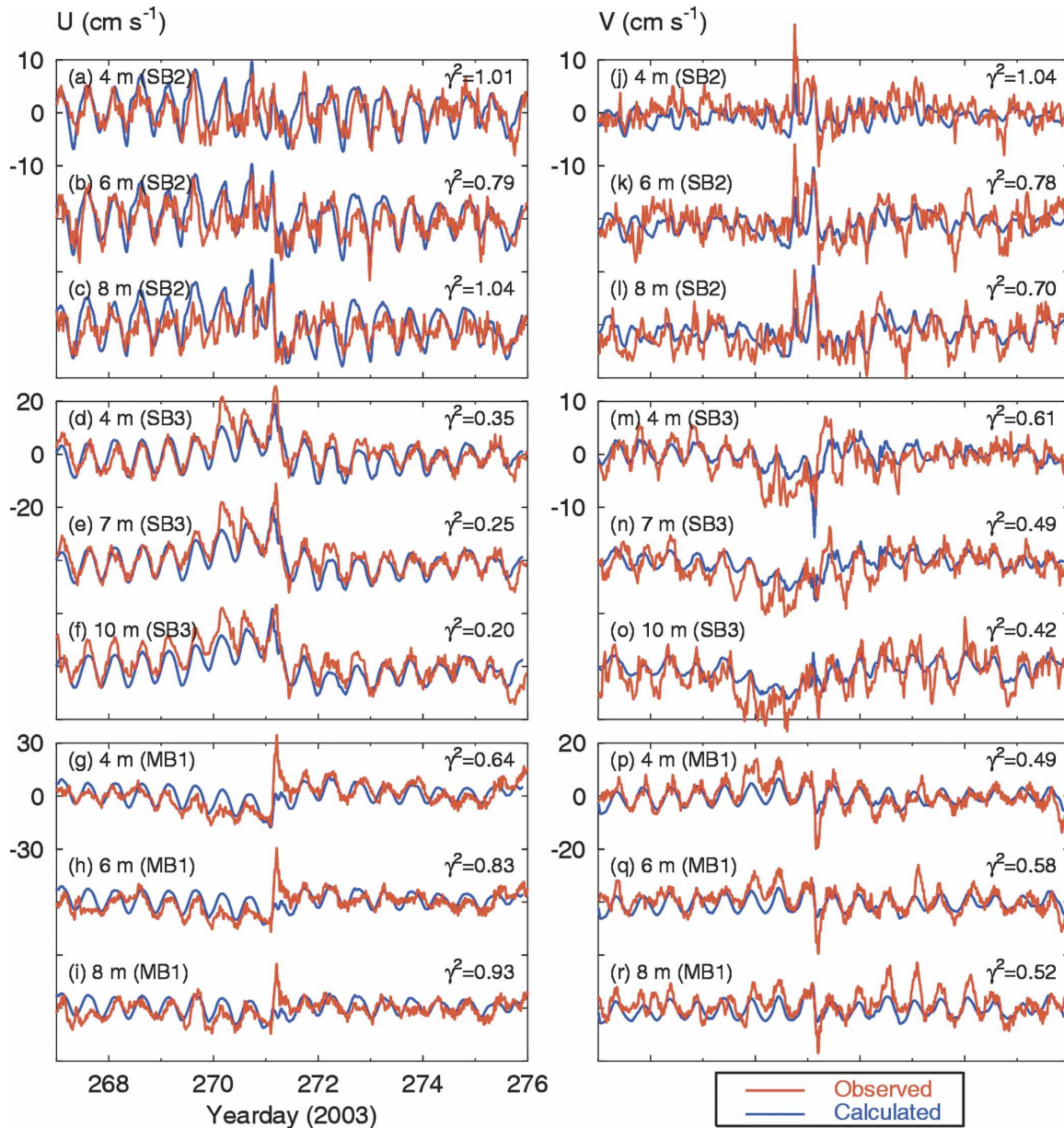


FIG. 9. Time series of (left) eastward and (right) northward components of observed (red) and simulated (blue) currents at depths of 4, 6, and 8 m for site (top) SB2; those at (middle) depths of 4, 7, and 10 m for site SB3, and those at depths (bottom) of 4, 6, and 8 m for site MB1.

tical mixing parameterizations. Although discussion of baroclinic effects are beyond the scope of this paper, it should be noted that vertical stratification in LB was very weak on days 271 and 272 because of strong vertical mixing associated with Hurricane Juan, and relatively stronger before and after the storm as indicated by the temperature and salinity observations at site SB3. The other important factor is radiation stress associated with surface waves. The wave rider buoy deployed to the south of Cross Island detected large sur-

face waves during Hurricane Juan, with a maximum observed wave height of about 9 m in the early morning of 29 September. Therefore, the large discrepancies between the observed and simulated currents on day 271 (the observed sharp flow reversal and strong southeastward flow at MB1 near day 271.2 in Fig. 9) could be associated with the additional currents generated by the radiation stress of surface waves. Furthermore, an examination of Fig. 4 indicates that there is substantial eddy variability during the outer flow in the area near

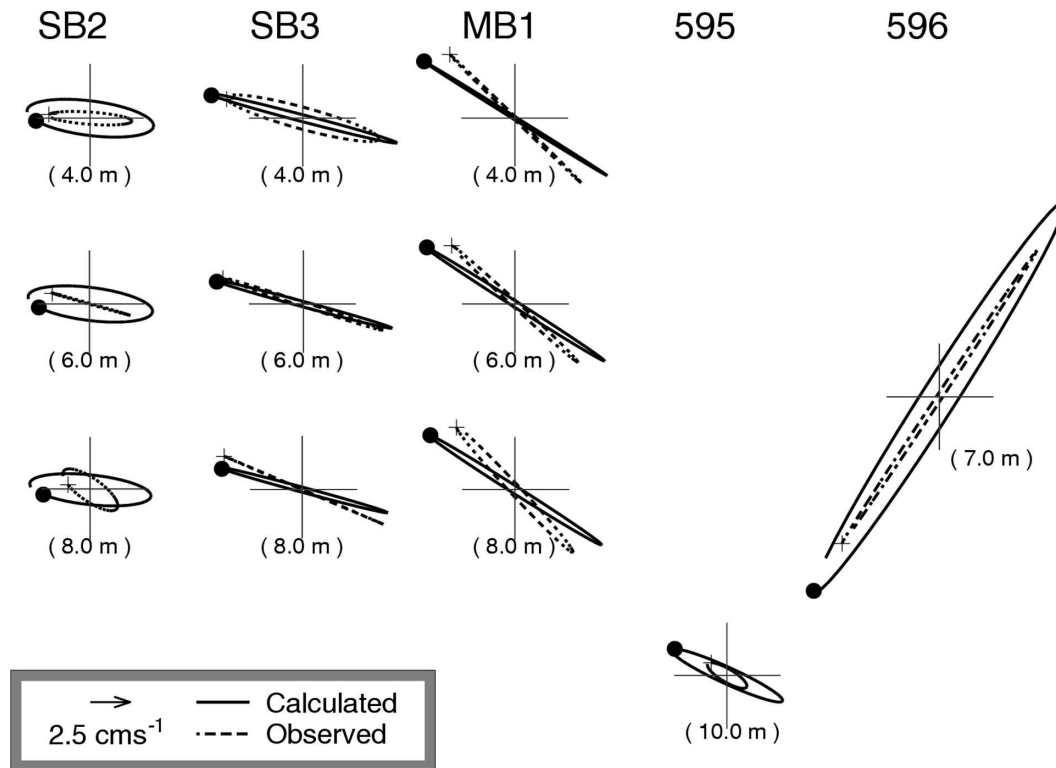


FIG. 10. Comparison of observed and simulated M_2 tidal ellipses at depths of 4, 6, and 8 m for sites SB2, SB3, and MB1, at 10 m for site 595, and at 7 m for site 596.

MB1, which is generally difficult to simulate deterministically. Figure 9 also demonstrates that the observed currents at SB2 have significant high-frequency oscillations in comparison with the observed currents at the other two sites, for which the exact reason is unclear.

Tidal analyses of the observed and simulated currents (Fig. 9) indicate that the semidiurnal tidal flow is the predominant constituent of the total tidal currents in LB, which is also consistent with the previous findings of Sheng and Wang (2004). To validate the model performance in simulating tidal and nontidal currents, we decompose the observed and simulated currents shown in Fig. 9 into the tidal and nontidal currents using a MATLAB program known as T_TIDE (Pawlowicz et al. 2002). (Nontidal currents are defined as the differences between the total currents and tidal components estimated by T_TIDE). The observed and simulated semidiurnal M_2 current ellipses are compared in Fig. 10. The observed M_2 tidal currents are nearly rectilinear and aligned roughly with the bottom topography at sites SB3, MB1, and 595 (but not at 596 where the currents are strongly affected by the jetlike flow through Corkum's Channel, see section 7a for more discussion), with typical speeds of about 11 cm s^{-1} at 7 m depth of site 596, 6 cm s^{-1} at three depths

of sites SB3 and MB1, and 1.5 cm s^{-1} at 10 m of site 595. At site SB2, the observed M_2 tidal currents are about 3 cm s^{-1} and have relatively larger ellipticity than those at other sites, mainly because of the influence of the jetlike flow emanating from LSC to inner LB through Corkum's Channel. (We obtain very similar tidal current ellipses from the observed and simulated currents of the one-month period from 20 September to 20 October.) Overall, the coastal model reproduces reasonably well the orientation and ellipticity of the observed tidal current ellipses at the five sites, with the agreement between the simulated and observed M_2 tidal ellipses at SB3 and 596 to be marginally better than that at SB2 and 595. At MB1, there are systematic orientation differences between the observed and simulated M_2 tidal current ellipses at three depths, which could be attributed mainly to the inaccuracies in the model topography at this site.

A comparison between observed and simulated nontidal flows at SB3 (middle panels of Fig. 11) demonstrates that the LB coastal model also reproduces reasonably well the observed nontidal flows at this site, particularly the southeastward nontidal flow on days 270 and 271. This southeastward nontidal flow is primarily associated with the local wind forcing and asso-

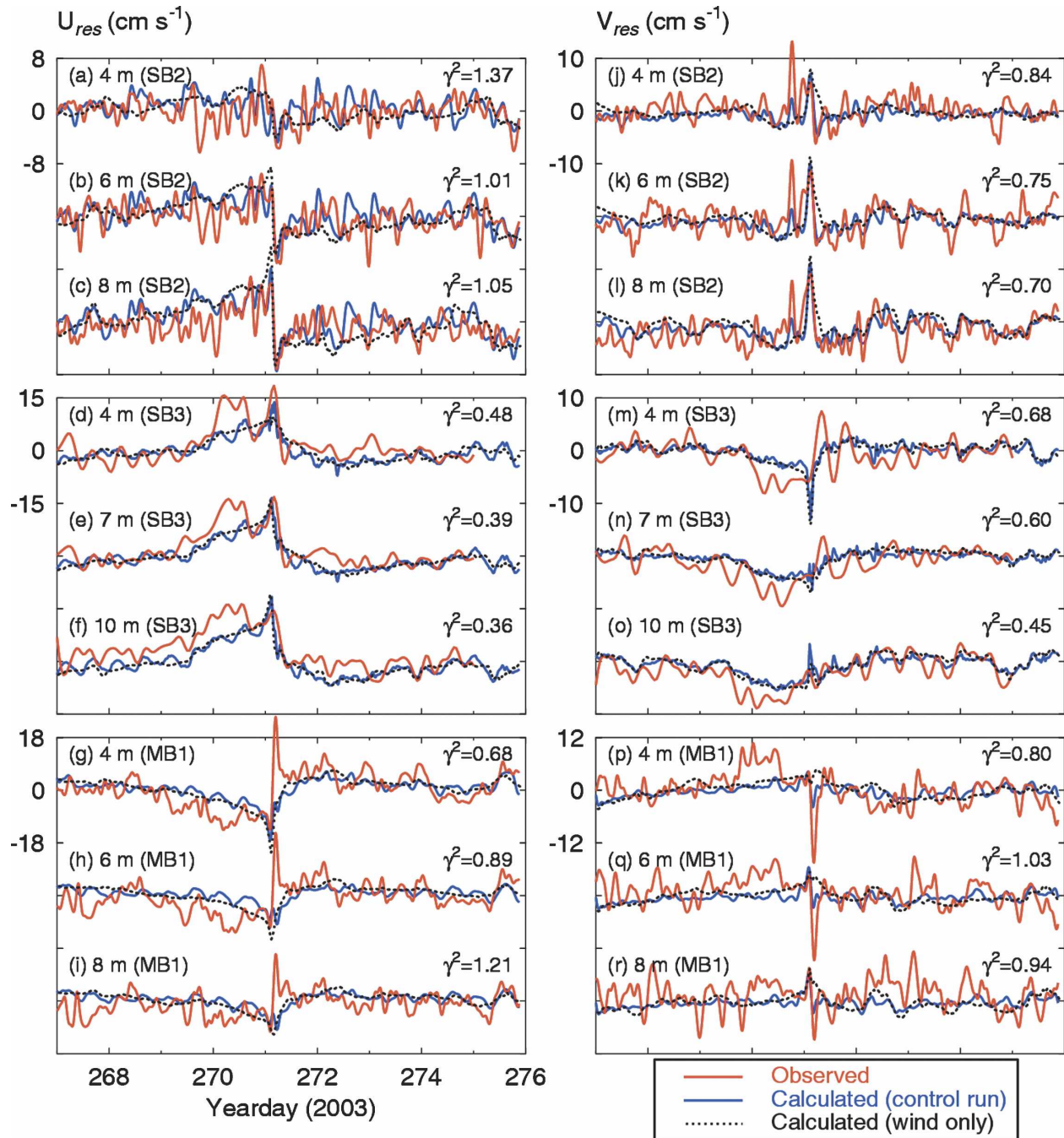


FIG. 11. Time series of (left) eastward and (right) northward components of observed (red) and simulated (blue) nontidal currents at depths of 4, 6, and 8 m for site (top) SB2; those at depths (middle) of 4, 7, and 10 m for site SB3, and those at depths (bottom) of 4, 6, and 8 m for site MB1. Dotted lines represent the model results forced by the local wind forcing only in Exp-C.

ciated pressure gradients on these two days (Fig. 3). The range of γ^2 values is 0.36–0.48 (0.45–0.68) for the eastward (northward) components of the nontidal currents at SB3 during the 9-day period. The γ^2 range is 1.01–1.37 (0.70–0.84) for the eastward (northward) components of the nontidal currents at SB2 (up-

per panels of Fig. 11), and 0.68–1.21 (0.80–1.03) for the eastward (northward) components at MB1 (lower panels of Fig. 11), which are larger than those at SB3. Figure 11 also demonstrates that the coastal model performs less well in simulating the observed nontidal flow at SB2 than that at SB3 and MB1 before and after

Hurricane Juan. The coastal model, however, reproduces realistically large temporal changes in the observed nontidal currents at SB2 during Hurricane Juan in the early morning of day 271. It should be noted that site SB2 is very close to the path of the jet flow that runs northeastward from Corkum's Channel to inner LB, and this jetlike flow occasionally spreads over this site. The observed nontidal currents at SB2 have a strong northward flow of about 10 cm s^{-1} at day 270.78 (upper-right panels of Fig. 11). This northward flow was not generated directly by Hurricane Juan wind since it appears about 6 h before the peak wind stress (see more discussions in section 7). The large discrepancies between the observed and simulated nontidal currents at SB3 and MB1 could largely be explained by the baroclinic effect in the bay on days 269 and 270 and radiation stress of surface waves on day 271.

Figure 11 also demonstrates that a major portion of the variance of the nontidal currents in the control run (Exp-A) can be accounted for by the model results forced by the local wind in Exp-C. There are noticeable differences, however, between the nontidal currents produced by the control run and the wind-driven results in Exp-C, particularly at SB2 and MB1 during Hurricane Juan. These differences indicate the likely importance of nonlinear interaction between the tidal- and wind-driven currents in the bay. More discussion of this topic is given in the next section.

6. Analysis of dynamic balance and nonlinear interaction

Sheng and Wang (2004) examined the tidal circulation and associated nonlinear dynamics over western LB, Corkum's Channel, and adjacent areas. In this section, we examine the effects of nonlinear dynamics on the storm-induced circulation in LB during Hurricane Juan based on the vertically averaged momentum equations defined as

$$\left\langle \frac{\partial u}{\partial t} \right\rangle + \langle \mathcal{L}u \rangle - \langle Fv \rangle = \left\langle -g \frac{\partial \eta}{\partial x} \right\rangle + \langle D_m u \rangle + \frac{\tau_x^s - \tau_x^b}{\rho_0 h} \quad \text{and} \quad (6)$$

$$\left\langle \frac{\partial v}{\partial t} \right\rangle + \langle \mathcal{L}v \rangle + \langle Fu \rangle = - \left\langle -g \frac{\partial \eta}{\partial y} \right\rangle + \langle D_m v \rangle + \frac{\tau_y^s - \tau_y^b}{\rho_0 h}, \quad (7)$$

where $\langle \rangle = (h + \eta)^{-1} \int_{-h}^{\eta} dz$, $\partial x = R \cos \phi \partial \lambda$, $\partial y = R \partial \phi$, and (τ_x^s, τ_y^s) and (τ_x^b, τ_y^b) are the eastward and northward components of surface wind and bottom stresses,

respectively. Other symbols in (6) and (7) are defined in the appendix.

Figure 12 shows time series of the depth-mean momentum terms calculated from model results at sites SB3 and 596 during Hurricane Juan from day 270.8 to 271.65 in the control run (Exp-A; Table 1). At site SB3, the depth-mean momentum balance in the eastward direction is primarily between the surface pressure gradient, $\langle -g \partial \eta / \partial x \rangle$, and difference between the surface wind stress and bottom stress, $(\tau_x^s - \tau_x^b) / \rho_0 h$, with some contributions from the nonlinear advection, $\langle \mathcal{L}u \rangle$, and local acceleration, $\langle \partial u / \partial t \rangle$, before day 271 (Fig. 12a). The depth-mean momentum balance is primarily between the surface pressure gradient, advection, and difference between the surface and bottom stress from day 271.05 and 271.15 and between the local acceleration, advection, and surface pressure gradient after day 271.15. The horizontal mixing, $\langle D_m u \rangle$, and Coriolis term, $\langle -Fv \rangle$, only play a minor role in the eastward direction at this site during Hurricane Juan. In the northward direction at SB3 (Fig. 12b), all the dynamic terms except for the horizontal mixing term contribute significantly to the momentum balance during the storm from day 271 and 271.2, with significant contributions from the nonlinear advection term, $\langle \mathcal{L}u \rangle$, around day 271.1.

At site 596 located at the eastern entrance of Corkum's Channel, the depth-mean momentum balance in the eastward direction is primarily between the pressure gradient, advection, and difference between the surface and bottom stress before day 271.1; between the pressure gradient, difference between the surface and bottom stress, and local acceleration from day 271.1 and 271.15; and between the nonlinear advection and pressure gradient after day 271.15 (Fig. 12c). In particular, the nonlinear advection term plays a very important role at day 271.2, which has the same amplitude as the pressure gradient term, and much larger than other four terms in amplitude. In the northward direction at site 596 (Fig. 12d), the pressure gradient term plays a dominant role before day 271.15 and after day 271.4. During these two periods, the pressure gradient is balanced primarily by local acceleration, advection, and difference between the surface and bottom stress. The nonlinear advection term plays a dominant role around day 271.2, which is balanced primarily by difference between the surface and bottom stress, local acceleration, and Coriolis term. Same as at SB3, the horizontal mixing plays only a minor role in the depth-mean momentum balance at site 596.

We next examine the nonlinear interaction of tidal, wind-driven, and RGW-induced currents in LB during Hurricane Juan based on the model results in four

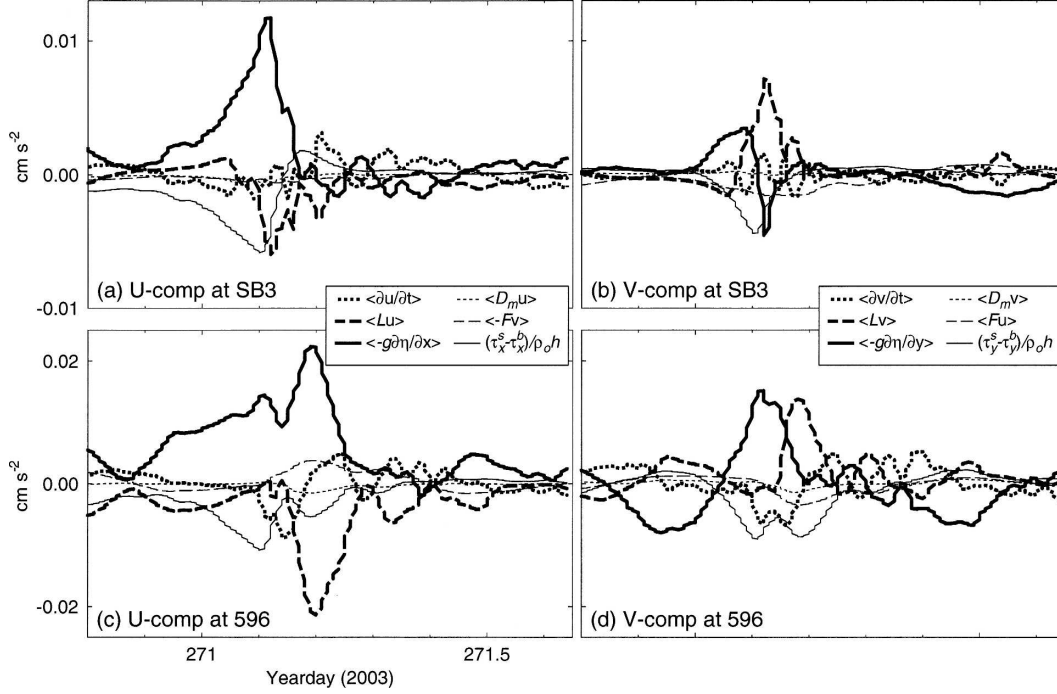


FIG. 12. Time series of dynamic terms in vertically averaged momentum equations in the eastward and northward directions from day 270.80 to 271.65 during Hurricane Juan at site SB3 and 596. Positive values are (a), (c) eastward and (b), (d) northward.

numerical experiments listed in Table 1. To quantify the nonlinear interaction, we calculate differences of surface elevations and currents from model results based on

$$\Delta\eta = \eta_c - \eta_t - \eta_w - \eta_r \quad \text{and} \quad (8)$$

$$\Delta\mathbf{u} = \mathbf{u}_c - \mathbf{u}_t - \mathbf{u}_w - \mathbf{u}_r, \quad (9)$$

where η_c and \mathbf{u}_c are the model-calculated surface elevations and currents forced by the combination of tides, local wind, and RGW in Exp-A (control run; Table 1), η_t and \mathbf{u}_t are those forced by the tidal forcing only in Exp-B, η_w and \mathbf{u}_w are those forced by the local wind forcing only in Exp-C, and η_r and \mathbf{u}_r are those forced by the RGW only in Exp-D. Since the RGW-induced currents are relatively small in comparison with tidal and wind-driven currents during Hurricane Juan (section 4), large values of $|\Delta\mathbf{u}|$ represent strong interaction of the tidal and wind-driven currents in the study region.

Before and after Hurricane Juan, both $\Delta\eta$ and $|\Delta\mathbf{u}|$ are very small, indicating the nonlinear interaction of the tidal, wind-driven, and RGW-induced currents is negligible in the bay for these periods. During the storm, $\Delta\eta$ remains small and only about a few centimeters in amplitude (not shown), indicating that the nonlinear interaction has insignificant effects on surface elevations in LB during this period. In comparison, $|\Delta\mathbf{u}|$ is

relatively large with significant temporal and spatial variability (Fig. 13), indicating the importance of the nonlinear interaction between the tidal and wind-driven currents in LB during Hurricane Juan. In the early morning of 29 September 2003 at 0006 UTC, the near-surface $|\Delta\mathbf{u}|$ is relatively small and less than 5 cm s^{-1} over most areas in LB (Fig. 13a), except for inner LB where $|\Delta\mathbf{u}|$ is greater than 10 cm s^{-1} . At 0230 UTC when local wind stress reached a maximum and turned approximately southwestward, large values of $|\Delta\mathbf{u}|$ occur not only along Corkum's Channel and over western LB, but also over outer LB and adjacent areas (Fig. 14b). At 0454 UTC, at which time the local wind decreased to 0.23 N m^{-2} and η_s was negligible, the near-surface $|\Delta\mathbf{u}|$ still has much large values over the most areas of LB, including Corkum's Channel, inner LB and western LB (Fig. 13c). At 0718 UTC, the local wind stress became very weak and the near-surface $|\Delta\mathbf{u}|$ is relatively small in Corkum's Channel and over eastern LB but remains large in the western LB and south-east LB (Fig. 13d).

7. Sensitivity studies

a. Effect of local wind stress

As mentioned in section 3, the local wind forcing used in the control run is assumed to be spatially uni-

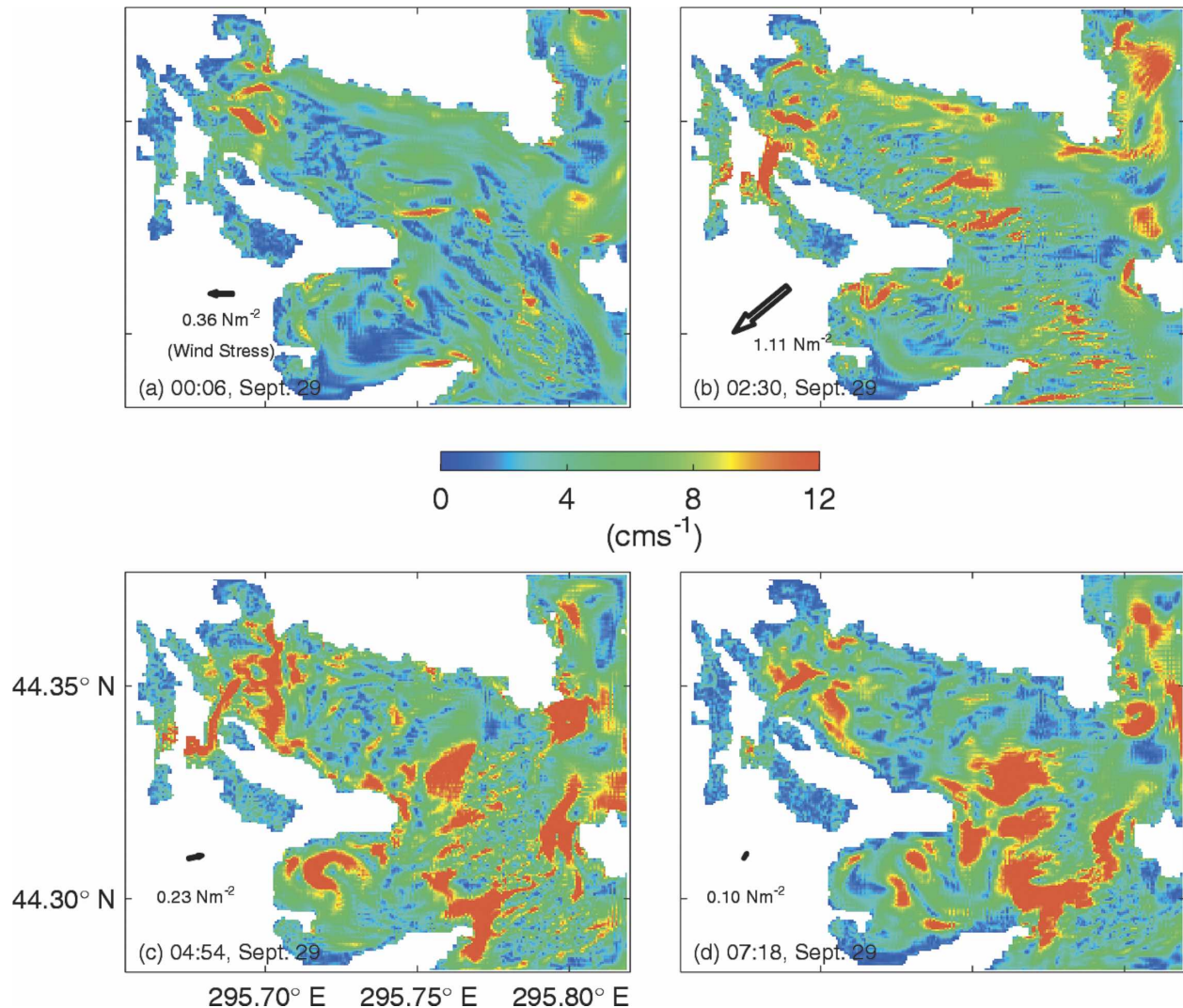


FIG. 13. Velocity difference magnitudes, representing the effect of nonlinear terms in the model on the predicted currents [see (9) and related text], in the top z level (1.8 m) at (a) 0006, (b) 0230, (c) 0454, and (d) 0718 UTC 29 Sep (day 271) 2003.

form and equal to the area-mean wind stress averaged from observed wind stresses (converted from the observed wind speeds) at two sites SB2 and SB3 in LB. The observed wind stresses at the two sites are highly similar throughout the 10-day study period. However, there are some noticeable differences between them before and during Hurricane Juan. To examine how the circulation in LB is affected by differences in wind stress, we conduct two numerical experiments and force the coastal model with the observed wind stress at SB2 in the first experiment (Exp-E) and with the observed wind stress at SB3 in the second (Exp-F). Other model forcing and parameters are the same as in the control run.

The large-scale circulation features in LB in the two experiments (not shown) are highly similar, which is

expected. There are significant differences, however, in small-scale circulation features between the two experiments. Figures 14a,b demonstrate that the use of different wind stresses leads to differences in the ebb-tide jet flowing from Corkum's Channel into inner LB. The velocity core of the jet shifts north and affects the simulated flow at site SB2 if the observed wind stress at site SB3 is used to drive the coastal model (Exp-F). In comparison, the jetlike flow does not affect very much the simulated currents at site SB2 if the observed wind stress at SB2 is used (Exp-E). Figures 14c,d demonstrate that the use of observed wind stress at SB3 improves the agreement between the observed and simulated currents at day 271.78. It should be noted, however, that the model results with the use of the observed wind stress at SB3 are not always better than those with

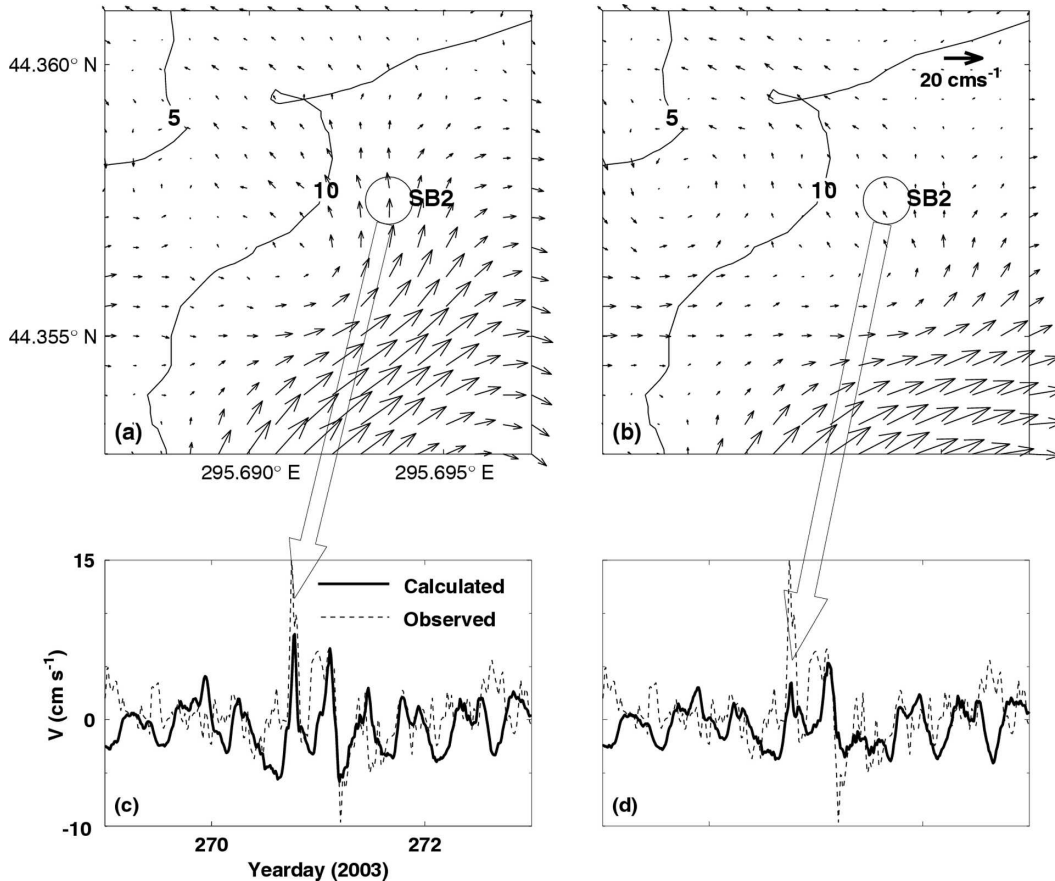


FIG. 14. Near-surface currents predicted for inner Lunenburg Bay in the vicinity of site SB2, using different observed winds. The results obtained using (a) SB3 and (b) SB2 winds at day 270.78. Time series of the observed (dashed) and predicted (solid) northward component of the current at 4-m depth are plotted for (c), (d) site SB2. (c) The model was driven with the observed wind stress at site SB3, as in (a). Similarly, in (d) the model used the winds at site SB2, as in (b). The contour lines in (a) and (b) denote the 5- and 10-m depth contours.

the use of the observed wind stress at SB2 during the whole study period.

b. Effect of vertical mixing

Ocean circulation models that do not resolve finescale turbulence usually require parameterizations of horizontal and vertical subgrid-scale mixing. As indicated in (1), a linear combination of wind-induced (K_w) and tide-induced (K_t) schemes is used in the control run for the vertical eddy viscosity coefficient (K_m). To examine the sensitivity of the model results to this vertical mixing scheme, we conduct two numerical experiments by forcing the model with $K_m = K_t$ in the first experiment (Exp-G), and $K_m = K_w$ in the second experiment (Exp-H).

Figure 15 demonstrates that, at the head of the Bay (site SB2), the model in Exp-G with tidal mixing only ($K_m = K_t$) reproduces reasonably well the observed

currents before and after Hurricane Juan, but performs less well during Hurricane Juan. In contrast, with wind mixing only ($K_m = K_w$) the model in Exp-H reproduces reasonably well the observed currents at SB2 during Hurricane Juan, but less well in simulating the observed currents before and after the hurricane. At sites SB3 and MB1, however, differences in the model-calculated currents between the two experiments are generally small before and after Hurricane Juan; major differences only occur during the storm.

A comparison of horizontal distributions of model surface currents in the two experiments (not shown) demonstrates that the model currents during the hurricane are much more energetic with tidal mixing only (Exp-G), than with wind mixing only (Exp-H). The higher currents in Exp-G are expected, because less wind energy is transferred from the top z level to other z levels in the former case, because of weaker vertical

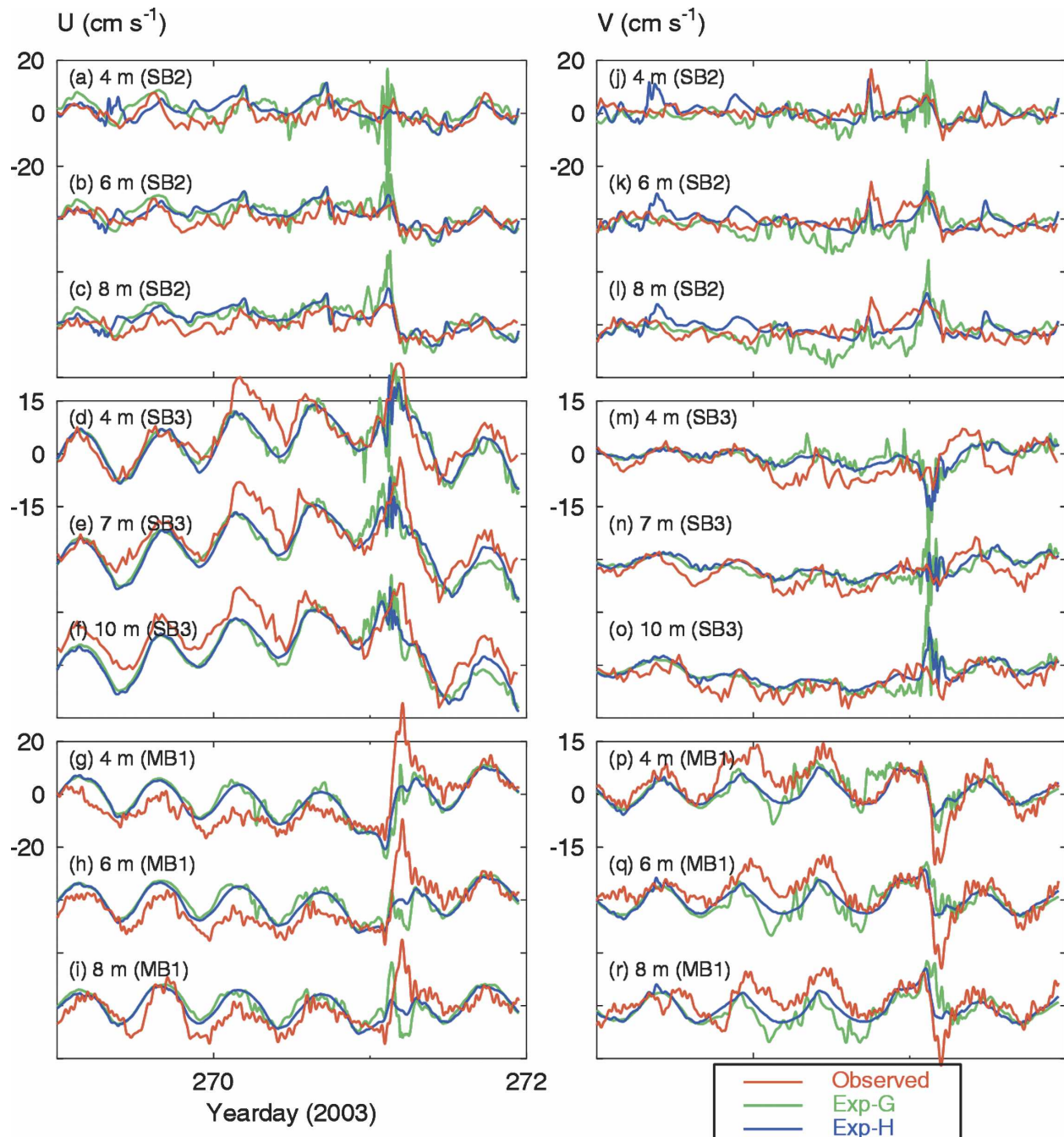


FIG. 15. Time series of (left) eastward and (right) northward components of observed (red) and simulated (blue) currents at depths of 4, 6, and 8 m for (top) site SB2; those at depths of 4, 7, and 10 m for (middle) site SB3, and those (bottom) at depths of 4, 6, and 8 m for site MB1. The model results are generated using different vertical mixing schemes. The vertical eddy viscosity coefficient is set to the tide-induced scheme ($K_m = K_t$) in Exp-G, and to the wind-induced scheme ($K_m = K_w$) in Exp-H.

mixing. Thus, a slower dissipation of the kinetic energy in the flow is expected in Exp-G than in Exp-H.

8. Summary and discussion

Oceanographic observations under extreme weather conditions such as hurricanes and winter storms are

very difficult to make and therefore rare. We documented in this paper that continuous and high-quality observations were registered by a coastal observatory established in Lunenburg Bay (LB) of Nova Scotia, when a category-2 hurricane (Juan) made a landfall within 50 km of the site in September of 2003. Only the

observed surface winds, surface elevations, and currents made by the observatory were presented in this study. Discussion of other observed variables, such as temperature and salinity, will be presented elsewhere.

We demonstrated in this paper that the z -level ocean circulation model known as CANDIE, with a horizontal resolution of about 60 m and vertical resolution of about 1 to 5 m, is capable of simulating the 3D circulation in LB and associated coves. We quantified the model performance by comparing the model results with the observations made in the bay during Hurricane Juan. The z -level coastal circulation model reproduces very well the observed surface elevations with γ^2 values of less than 0.05 in the bay during Hurricane Juan. The coastal model, however, reproduces less well the observed currents with γ^2 values between 0.20 and 1.04 during the same period. It is likely that discrepancies between the observed and simulated currents during the storm could be explained partially by wave-current interactions, and partially by the baroclinic effects.

The model results were also used to examine the nonlinear dynamics of the coastal circulation forced by tides, wind and RGW forcing in the bay. An examination of vertically averaged momentum equations at two sites in Lunenburg Bay demonstrates the importance of the nonlinear advection, surface pressure gradient, local acceleration, surface wind stress and bottom friction in generating the storm-induced circulation in Lunenburg Bay during Hurricane Juan. In comparison, the horizontal mixing and Coriolis term play only a minor role in the vertically averaged momentum balance at the two sites.

Based on the comparison of observed and simulated surface elevations and coastal currents in LB during Hurricane Juan, we conclude that the surface elevations in the bay were simulated accurately during the storm, but are not sensitive indicators of assessing the performance of the LB model. The three-dimensional

coastal currents in the bay were simulated less well, mainly because of the complexity of temporal and spatial variations in the response of the bay to local wind forcing. (It should also be noted that there are spatially coherent and temporally persistent circulation features in the bay produced by the model.) One of the consequences of the complexity is large spatial gradients of the currents in the bay, which explains why the nonlinear advective terms contribute significantly to the momentum balance. These large spatial gradients also complicate the model-data comparisons. In addition, the velocity gradients are partially controlled by the bathymetry, and thus the model-data comparisons in high velocity gradient zones will be sensitive to the representation of the bathymetry in the model.

Acknowledgments. We thank Li Zhai, Jun Zhao, Richard Greatbatch, Mike Dowd, Harold Ritchie, Tony Bowen, Chris Fogarty, John Cullen, and Keith Thompson for their useful suggestions. We also thank Charles O'Really for providing the sea level tidal prediction at Lunenburg Harbour. This project is part of the CMEP project supported by the Canadian Foundation for Climate and Atmospheric Studies (CFCAS). Author J.S. is also supported by NSERC, MARTEC (a Halifax-based company), and the Meteorological Service of Canada (MSC) through the NSERC/MARTEC/MSC Industrial Research Chair in "Regional Ocean Modelling and Prediction."

APPENDIX

Basic Equations of the Ocean Circulation Model

The three-dimensional primitive equation ocean circulation model known as CANDIE (<http://www.phys.ocean.dal.ca/programs/CANDIE>; Sheng et al. 1998; Sheng et al. 2001a; Lu et al. 2001) with a free surface is used in this study. The governing equations of the model can be written in spherical coordinates as

$$\frac{\partial u}{\partial t} + \mathcal{L}u - Fv = -\frac{g}{R \cos\phi} \frac{\partial(\eta + p_b/\rho_0 g)}{\partial \lambda} + \mathcal{D}_m u + \frac{\partial}{\partial z} \left(K_m \frac{\partial u}{\partial z} \right), \quad (\text{A1})$$

$$\frac{\partial v}{\partial t} + \mathcal{L}v + Fu = -\frac{g}{R} \frac{\partial(\eta + p_b/\rho_0 g)}{\partial \phi} + \mathcal{D}_m v + \frac{\partial}{\partial z} \left(K_m \frac{\partial v}{\partial z} \right), \quad (\text{A2})$$

$$\frac{\partial \eta}{\partial t} = -\frac{1}{R \cos\phi} \left[\frac{\partial \int_{-h}^{\eta} u \, dz}{\partial \lambda} + \frac{\partial \left(\int_{-h}^{\eta} v \cos\phi \, dz \right)}{\partial \phi} \right], \quad (\text{A3})$$

$$\frac{\partial w}{\partial z} = -\frac{1}{R \cos\phi} \left[\frac{\partial u}{\partial \lambda} + \frac{\partial(v \cos\phi)}{\partial \phi} \right], \quad \text{and} \quad (\text{A4})$$

$$p_b = g \int_z^\eta \rho dz', \quad (\text{A5})$$

where u , v , and w are the east (λ), north (ϕ), and vertical (z) components of the velocity vector \mathbf{u} , η is the surface elevation, $z = -h(x, y)$ is the position of the sea bottom, p is pressure, ρ is density, T and S are the potential temperature and salinity, p_b is the density-driven internal pressure, K_m is the vertical eddy viscosity coefficient, $F = f + u \tan\phi/R$, f is the Coriolis parameter, ρ_0 is a reference density, R and g are the earth's radius and gravitational acceleration, and \mathcal{L} is an advection operator defined as

$$\mathcal{L}q = \frac{1}{R \cos\phi} \frac{\partial(uq)}{\partial\lambda} + \frac{1}{R \cos\phi} \frac{\partial(vq \cos\phi)}{\partial\phi} + \frac{\partial(wq)}{\partial z}. \quad (\text{A6})$$

Diffusion operator \mathcal{D}_m is defined as

$$\mathcal{D}_m q = \frac{1}{R^2} \left[\frac{1}{\cos^2\phi} \frac{\partial}{\partial\lambda} \left(A_m \frac{\partial q}{\partial\lambda} \right) + \frac{\partial}{\partial\phi} \left(\cos\phi A_m \frac{\partial q}{\partial\phi} \right) \right], \quad (\text{A7})$$

where A_m is the horizontal eddy viscosity coefficient. The model also uses the fourth-order numerics (Dietrich 1997) and Thuburn's flux limiter to discretize the nonlinear advection terms (Thuburn 1996).

REFERENCES

- Anderson, C., and P. C. Smith, 1989: Oceanographic observations on the Scotian Shelf during CASP. *Atmos.–Ocean*, **27**, 130–156.
- Bobanovic, J., and K. R. Thompson, 2001: The influence of local and remote winds on the synoptic sea level variability in the Gulf of Saint Lawrence. *Cont. Shelf Res.*, **21**, 129–144.
- Chapman, D. C., 1985: Numerical treatment of cross-shelf open boundaries in a barotropic coastal ocean model. *J. Phys. Oceanogr.*, **15**, 1060–1075.
- Csanady, G. T., 1982: *Circulation in the Coastal Ocean*. D. Reidel Publishing, 279 pp.
- Davidson, F. J. M., R. J. Greatbatch, and B. deYoung, 2001: Asymmetry in the response of a stratified coastal embayment to wind forcing. *J. Geophys. Res.*, **106**, 7001–7016.
- Davies, A. M., 1993: A bottom boundary layer-resolving three-dimensional tidal model: A sensitivity study of eddy viscosity formulation. *J. Phys. Oceanogr.*, **23**, 1437–1453.
- , and R. A. Flather, 1978: Computing extreme meteorologically induced currents, with application to the northwest European continental shelf. *Cont. Shelf Res.*, **7**, 643–683.
- , S. C. M. Kwong, and R. A. Flather, 1998: A three-dimensional model of wind-driven circulation on the shelf: Application to the storm of January 1993. *Cont. Shelf Res.*, **18**, 289–340.
- de Young, B., T. Otterson, and R. J. Greatbatch, 1993: The local and nonlocal response of Conception Bay to wind forcing. *J. Phys. Oceanogr.*, **23**, 2636–2649.
- Dietrich, D. E., 1997: Application of a modified Arakawa “a” grid ocean model having reduced numerical dispersion to the Gulf of Mexico circulation. *Dyn. Atmos. Oceans*, **27**, 201–217.
- Gill, A. E., 1982: *Atmosphere–Ocean Dynamics*. Academic Press, 662 pp.
- Grant, J., M. Dowd, K. Thompson, C. Emerson, and A. Hatcher, 1993: Perspectives on field studies and related biological models of bivalve growth and carrying capacity. *Bivalve Filter Feeders and Marine Ecosystem Processes*, R. Dame, Ed., Springer-Verlag, 371–420.
- Greenberg, D. A., J. W. Loder, Y. Shen, D. R. Lynch, and C. E. Naimier, 1997: Spatial and temporal structure of the barotropic response of the Scotian Shelf and Gulf of Maine to surface wind stress: A model-based study. *J. Geophys. Res.*, **102**, 20 897–20 915.
- Griffin, D. A., and K. R. Thompson, 1996: The adjoint method of data assimilation used operationally for shelf circulation. *J. Geophys. Res.*, **101**, 3457–3477.
- Large, W. G., and S. Pond, 1981: Open ocean momentum flux measurements in moderate to strong winds. *J. Phys. Oceanogr.*, **11**, 324–336.
- Levinson, D. H., and A. M. Waple, 2004: State of the climate in 2003. *Bull. Amer. Meteor. Soc.*, **85**, 881.
- Lu, Y., K. R. Thompson, and D. G. Wright, 2001: Tidal currents and mixing in the Gulf of St. Lawrence: An application of the incremental approach to data assimilation. *Can. J. Fish. Aquat. Sci.*, **58**, 723–735.
- Pawlowicz, R., B. Beardsley, and S. Lentz, 2002: Classical tidal harmonic analysis including error estimates in MATLAB using T_TIDE. *Comput. Geosci.*, **28**, 929–937.
- Safer, A., 2002: MEPS: A prototype for the study of coastal dynamics. *Sea Technol.*, **40**, 10–14.
- Schwing, F. B., 1992: Subtidal response of Scotian Shelf circulation to local and remote forcing. Part II: Barotropic model. *J. Phys. Oceanogr.*, **22**, 542–563.
- Sheng, J., 2001: Dynamics of a buoyancy-driven coastal jet: The Gaspé Current. *J. Phys. Oceanogr.*, **31**, 3146–3163.
- , and L. Tang, 2003: A numerical study of circulation in the western Caribbean Sea. *J. Phys. Oceanogr.*, **33**, 2049–2069.
- , and —, 2004: A two-way nested-grid ocean circulation model for the Meso-American Barrier Reef System. *Ocean Dyn.*, **54**, 232–242.
- , and L. Wang, 2004: Numerical study of tidal circulation and nonlinear dynamics in Lunenburg Bay, Nova Scotia. *J. Geophys. Res.*, **109**, C10018, doi:10.1029/2004JC002404.
- , D. G. Wright, R. J. Greatbatch, and D. E. Dietrich, 1998: CANDIE: A new version of the DieCAST ocean circulation model. *J. Atmos. Oceanic Technol.*, **15**, 1414–1432.
- , R. J. Greatbatch, and D. G. Wright, 2001a: Improving the utility of ocean circulation models through adjustment of the momentum balance. *J. Geophys. Res.*, **106**, 16 711–16 728.
- , K. R. Thompson, L. Cong, P. C. Smith, and D. L. Lawrence,

- 2001b: Effect of wind and local density on the subtidal circulation of the inner Scotian Shelf. *Cont. Shelf Res.*, **21**, 1–19.
- , X. Zhai, and R. J. Greatbatch, 2006: Numerical study of the storm-induced circulation on the Scotian Shelf during Hurricane Juan using a nested-grid ocean model. *Progress in Oceanography*, Vol. 70, Pergamon Press, 233–254.
- Smagorinsky, J., 1963: General circulation experiments with the primitive equation. Part I: The basic experiment. *Mon. Wea. Rev.*, **91**, 99–165.
- Smith, P. C., and F. B. Schwing, 1991: Mean circulation and variability on the eastern Canadian continental shelf. *Cont. Shelf Res.*, **11**, 977–1012.
- Sturley, D. R. M., K. R. Thompson, and A. J. Bowen, 1993: Fine-scale models of coastal inlets: A physical basis for water quality/biological models. *Proc. Canadian Coastal Conference*, Vancouver, BC, Canada, 387–404.
- Tang, C. L., Q. Gui, and B. M. DeTracey, 1998: Barotropic response of the Labrador/Newfoundland shelf to a moving storm. *J. Phys. Oceanogr.*, **28**, 1152–1172.
- Therriault, J.-C., and Coauthors, 1998: Proposal for a northwest Atlantic zonal monitoring program. Canadian Tech. Rep. of Hydrography and Ocean Sciences 194, 57 pp.
- Thompson, K. R., and J. Sheng, 1997: Subtidal circulation on the Scotian Shelf: Assessing the hindcast skill of a linear, barotropic model. *J. Geophys. Res.*, **102**, 24 987–25 003.
- , D. E. Kelley, D. Sturley, B. Topliss, and R. Leal, 1998: Near-shore circulation and synthetic aperture radar: An exploratory study. *Int. J. Remote Sens.*, **19**, 1161–1178.
- , J. Sheng, P. C. Smith, and L. Cong, 2003: Prediction of surface currents and drifter trajectories on the inner Scotian Shelf. *J. Geophys. Res.*, **108**, 3287, doi:10.1029/2001JC001119.
- Thuburn, J., 1996: Multidimensional flux-limited advection schemes. *J. Comput. Phys.*, **123**, 74–83.